Fabrication and Characterization of Thin Film Multilayer and Nanowire Metamaterials

by

Jonathan Atkinson

A thesis submitted in partial fulfillment of the requirements for the degree of

Master of Science
in
Photonics and Plasmas

Electrical and Computer Engineering
University of Alberta

Abstract

Metamaterials are artificially nano engineered materials with unique electromagnetic properties. They have applications in wave guiding, sensing, imaging, thermal, and quantum optics. Recently, metamaterials have been proposed as optical elements such as polarizers, analyzers, and diffraction gratings for on-chip photonic circuits. This thesis focuses on the design and characterization of 2D nanowire and 1D multilayer metamaterials for applications in wave guiding, sensing, and polarization manipulation.

We first report on the design, fabrication, and characterization of a straight gold nanowire structure with two unique plasmonic resonances. One resonance is omni directional and polarization insensitive while the second resonance is highly dependent on nanowire diameter and wire to wire spacing, ideal for sensing applications. Inclined gold nanowire metmaterials along with titanium dioxide inclined and helical nanowire structures are designed and characterized for polarization manipulation to be integrated as nano devices in photonic circuits. Horizontally inclined gold nanowires are shown to have strong anisotropy and manipulate the polarization state of light over a highly tunable narrow wavelength range.

The geometric phase is examined on the Poincaré Sphere and momentum space in optical fibers. A gold helical nanowire structure as a circular polarizer is introduced with a highly tunable resonance in the mid infrared range.

Finally, relaxed total internal reflection is experimentally shown by measuring the critical angle for total internal reflection by fabricating silica/silicon multilayer structures on hemicylindrical silicon prisms. The critical angle for total internal reflection is shown to be different for (p) and (s) polarized light. This experimental

work is the first evidence of relaxed total internal reflection.

This work paves the way for further advancements for waveguides and polarization manipulation elements for photonic circuits.

Preface

- A version of Chapter 1 has been published in Nano Convergence - P. Shekhar, J. Atkinson, and Z. Jacob, Hyperbolic Metamaterials: Fundamentals and Applications *Nano Convergence*, 1 (14) 2014.

- A version of Chapter 2.1 has been published in Journal of Optical Society of America B - R. Starko-Bowes, J. Atkinson, W. Newman, H. Hu, T. Kallos, G. Palikaras, R. Fedosejevs, S. Pramanik, and Z. Jacob, Optical characterization of epsilon-near-zero, epsilon-near-pole, and hyperbolic response in nanowire metamaterials *Journal of Optical Society of America B*, 32 (10): 2074-2080, 2015.

I would like to dedicate this work to my father, Peter Atkinson and my mother, Brenda Atkinson for always being there for support and guidance along the way.

Acknowledgments

There are many people I have to thank that have helped me with this work starting with my research group consisting of: Cris Cortes, Yu Guo, Huan Hu, Saman Jahani, Farid Kalhor, Sean Molesky, Ward Newman, Prashant Shekhar, and Ryan Starko-Bowes. Their help and support through criticism and discussion have helped me improve and move in the right direction with my academic career. More importantly though is their friendship I have gained through working together with them for the past three years.

Secondly, I would like to acknowledge Aaron Melnyk and Trevor Allen for their assistance in helping me learn the details of fabrication and characterization methods required to complete this work. I would also like to acknowledge Robert Winter for his contribution to the derivation of Geometric Phase using Stoke's Vectors.

Next, I would like to thank my supervisor, Dr. Zubin Jacob for acting not just as a supervisor but as a strong mentor and for believing in me through the completion of this work. His guidance and assistance in helping to solve problems has helped greatly finishing this work and improving as an individual.

Last but not least, I would like to thank my parents Peter and Brenda Atkinson, my sister Aislinn Atkinson, and my grandfather Ernie Atkinson for their guidance, patience and support through all my years of school.

Contents

List of Figures

List of Abbreviations and Symbols

Abbreviation	Extended Form
EMT	Effective Medium Theory
HMM	Hyperbolic Metamaterial
SPP	Surface Plasmon Polariton
λ	Wavelength
TIR	Total Internal Reflection
GLAD	Glancing Angle Deposition
TMM	Transfer Matrix Method
ENZ	Epsilon-Near-Zero
ENP	Epsilon-Near-Pole
TE	Transverse Electric
TM	Transverse Magnetic

Chapter 1

Introduction

1.1 Metamaterials

The field of metamaterials was first introduced when scientists and engineers began to search for materials that simultaneously had negative dielectric permittivity and negative magnetic permeability to achieve a negative refractive index material [5]. It was later found that the electromagnetic responses achieved from metamaterials could be used for more applications than just negative refractive index. The best example is cloaking where a metamaterial with an anisotropic electromagnetic response can be used to bend light smoothly around an object so it appears invisible [9, 30]. Research has also been done in sub-diffraction waveguiding [13], imaging [36, 14, 47], sensing [43], nano waveguiding [13], spontaneous [19] and thermal emission engineering [39]. Research in metamaterials began in the microwave regime of the electromagnetic spectrum [9] and has progressed to shorter wavelengths in the infrared and visible spectrum, enabled by advances in micro/nanofabrication techniques.

For materials found in nature, the radius of each atom and inter atomic spacing between atoms in the crystal structure of a material is much less than the wavelength of radiation (figure 1(a)) [34]. Metamaterials are composed of nano inclusions (or meta atoms) which are nano structures with critical dimensions much less than the wavelength of radiation, engineered to achieve unique and highly anisotropic electromagnetic responses (figure 1(b)) [34]. The unique electromagnetic responses arise from the near-field coupling between the sub wavelength building blocks. Recent improvements in the field of micro and nanofabrication have considerably improved the quality of the responses seen in the metamaterials.

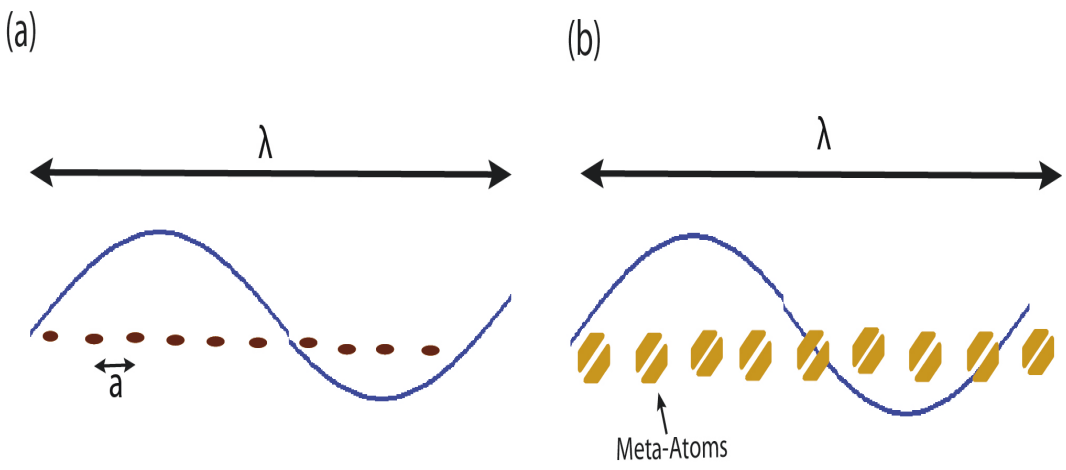

Figure 1.1: [34] (a) Periodic array of atoms with inter atomic spacing much less than the wavelength of light. (b) Metamaterials are composed of meta atoms which can be described as nano inclusions with critical dimensions much less than the wavelength of light.

1.2 Hyperbolic Metamaterials and K-space Topology

In an isotropic medium, the response of the medium to an electromagnetic field is the same in all directions and the electric permittivity is a scalar quantity. However, when a medium becomes anisotropic such that its electromagnetic response is different in the $\overrightarrow{x}$, $\overrightarrow{y}$, and $\overrightarrow{z}$ directions, the dielectric constant becomes a second degree tensor defined as

$$\overleftrightarrow{\epsilon} = \begin{pmatrix} \epsilon_{xx} & 0 & 0 \\ 0 & \epsilon_{yy} & 0 \\ 0 & 0 & \epsilon_{zz} \end{pmatrix}$$

where ϵ_{xx}, ϵ_{yy}, and ϵ_{zz} are the dielectric constants for the $\overrightarrow{x}$, $\overrightarrow{y}$, and $\overrightarrow{z}$ directions of the material. For a uniaxial medium (two directions of the electromagnetic response of the medium are different) the in-plane isotropic components are $\epsilon_{xx} = \epsilon_{yy} = \epsilon_{\parallel}$ and $\epsilon_{zz} = \epsilon_{\perp}$.

Hyperbolic Metamaterials are a specific type of metamaterial that get their name from the shape of their dispersion relation. In a conventional dielectric material ($\epsilon > 0$), the linear dispersion and isotropic behaviour imply that the isofrequency curve is a sphere. The isofrequency surface of a propagating wave with linear dispersion and isotropic behaviour can be derived from Maxwell's equations and is given by $k_x^2 + k_y^2 + k_z^2 = \frac{\omega^2}{c^2}$ (figure 1.2(a)) [34]. In this equation, the wave vector of a propagating wave is given by $\overrightarrow{k} = [k_x, k_y, k_z]$, ω is the frequency of operation, and c is the speed of light in vacuum. Solving Maxwell's equations for an extraordinary wave (TM or

(p) polarized) in an anisotropic uniaxial medium changes the isofrequency relation to

$$\frac{k_x^2 + k_y^2}{\epsilon_{zz}} + \frac{k_z^2}{\epsilon_{xx}} = \frac{\omega^2}{c^2} \tag{1.1}$$

The spherical isofrequency surface will be distorted to an ellipsoid for the anisotropic case. However, for extreme anisotropy such that $\epsilon_{\parallel} \bullet \epsilon_{\perp} < 0$ the isofrequency surface becomes a hyperbola as shown in figure 1.2(b) and 1.2(c) [34]. Such behaviour requires the medium to behave like a metal ($\epsilon < 0$) in one direction and a dielectric or insulator ($\epsilon > 0$) in another direction. Materials with these properties are not readily available in nature at optical or near-infrared frequencies and thus artificial nanostructures or metamaterials must be used to see these unique electromagnetic properties.

The most important property related to the hyperbolic metamaterial is the behaviour of extremely large wave vectors. In vacuum, wave vectors larger than the free space wave vector ($k_o = \omega/c$) are evanescent and decay away exponentially. In a hyperbolic metamaterial, these high-k wave vectors that carry sub-diffraction limit information can propagate to the far-field due to the shape of the isofrequency surface. These high-k propagating wave vectors can be infinitely large in the idealistic limit. This unique property allows hyperbolic metamaterials to be used in many device applications.

There are two classes of hyperbolic metamaterials (HMMs) introduced to help identify their unique properties. Type 1 HMMs have one component of the dielectric tensor negative ($\epsilon_{zz} < 0$; $\epsilon_{xx}, \epsilon_{yy} > 0$) while Type II HMMs have two components less than zero ($\epsilon_{zz} > 0$; $\epsilon_{xx}, \epsilon_{yy} < 0$). The isofrequency surface for Type I HMMs is shown in figure 1.2(b) and for Type II HMMs in figure 1.2(c) [34]. It is important to note that if all components of the dielectric tensor are negative, the medium behaves as a metal and if all the components are positive, the medium behaves as a dielectric or insulating material. The most striking difference between Type I and II HMMs is the hyperboloid isofrequency surfaces are one and two sheeted respectively. The Type II HMM is also highly reflective due to it having two components ($\overrightarrow{x}$ and $\overrightarrow{y}$) of the dielectric tensor being negative compared to Type I where only the $\overrightarrow{z}$ component is negative. HMMs can not be experimentally characterized, so we must look at the resonance responses to characterize the anisotropic permittivity.

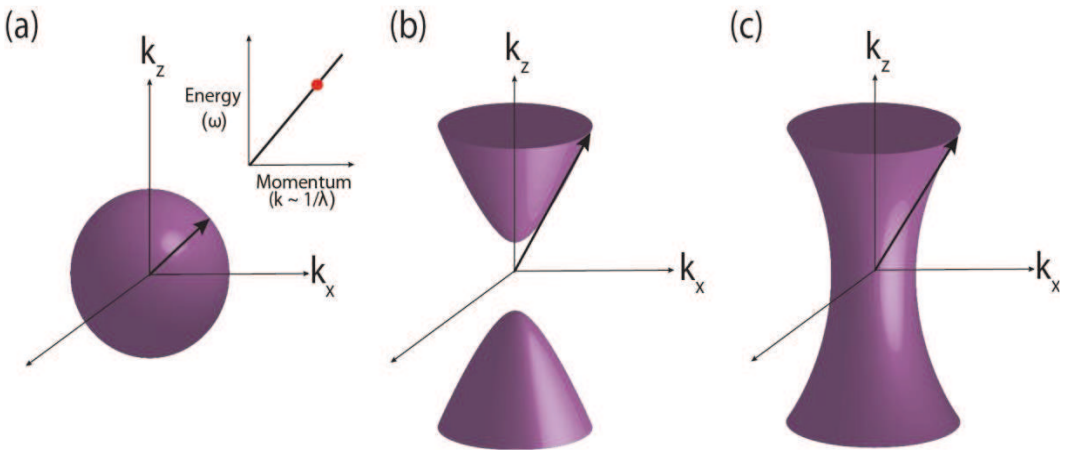

Figure 1.2: [34] (a) Spherical Isofrequency relation for an isotropic dielectric material. Inset is a plot of the linear relationship between energy and momentum with the red dot indicating the operating frequency for the constant frequency isofrequency surface. (b) Hyperboloid isofrequency surface for a Type I uniaxial medium with extremely large anisotropy (ϵ_{xx}; $\epsilon_{yy} > 0$; $\epsilon_{zz} < 0$). (c) Hyperboloid isofrequency surface for a Type II uniaxial medium with extremely large anisotropy (ϵ_{xx}; $\epsilon_{yy} < 0$; $\epsilon_{zz} > 0$).

1.3 Effective Medium Theory, Epsilon-Near-Zero (ENZ) and Epsilon-Near-Pole (ENP)

A numerical or theoretical model needs to be used to model the electromagnetic response of metamaterials due to the complexity of the medium for electric field excitations in the $\overrightarrow{x}$, $\overrightarrow{y}$, and $\overrightarrow{z}$ directions. For work in this thesis, the focus will be on 1D multilayer and 2D nanowire metamaterials that will be analyzed with homogenization. Homogenization involves determining the effective electromagnetic response of a metamaterial by averaging over the permittivities of its constituent components. This is possible when the critical dimensions of each meta atom are much less than the wavelength of radiation of excitation such that the magnitude of the electric field does not change significantly over the thickness of each structure. Figure 1.3 illustrates this process for multilayer metamaterials (figure1.3(a)) and nanowire metamaterials (figure1.3(b)). The metamaterial can therefore be considered as an effective medium and the permittivity of both the $\overrightarrow{x}$-$\overrightarrow{y}$ plane (parallel) and $\overrightarrow{z}$ (perpendicular) is found by using the Maxwell-Garnet approach. This method assumes an averaged displacement field and applying the appropriate boundary conditions. A detailed derivation can be found in the Appendix [34] for both the multilayer and nanowire structures. The final derived relations for a multilayer structure are:

$$\epsilon_{\parallel} = \epsilon_2 \rho + (1 - \rho)\epsilon_1 \tag{1.2}$$

$$\epsilon_{\perp} = \frac{\epsilon_1 \epsilon_2}{\rho \epsilon_2 + (1 - \rho)\epsilon_1} \tag{1.3}$$

where ρ (the fill fraction) for the multilayer case is defined as

$$\rho = \frac{d_1}{d_1 + d_2} \tag{1.4}$$

where ϵ_1 is the permittivity of material 1, ϵ_2 is the permittivity of material 2 and d_1 and d_2 are the thicknesses of material 1 (usually metal) and material 2 (usually dielectric). Similarly for a nanowire structure

$$\epsilon_{\parallel} = \frac{(1 + \rho)\epsilon_1 \epsilon_2 + (1 - \rho)\epsilon_2^2}{(1 + \rho)\epsilon_2 + (1 - \rho)\epsilon_1} \tag{1.5}$$

$$\epsilon_{\perp} = \rho \epsilon_1 + (1 - \rho)\epsilon_2 \tag{1.6}$$

where ρ for the nanowire case is defined as

$$\rho = \frac{nanowirearea}{unitcellarea} = \frac{na}{A} \tag{1.7}$$

where n is the number of nanowires per unit cell, a is the area of one nanowire, and A is the area of a unit cell which is taken to be a hexagon.

The characterization of artificial media and retrieval of effective medium parameters has been a controversial topic in the field of metamaterials. This primarily comes from the fact that unit cells are not deeply sub wavelength, the structures are two dimensional and the effective dielectric constant of the medium can not be strictly defined [34]. Metamaterials designed, fabricated, and characterized in this thesis do not suffer from these setbacks. Both 1D and 2D HMMs are deeply sub wavelength, the meta atoms are three dimensional, and the effective permittivity shows extreme anisotropy for TM or (p) polarized light.

If we examine equations 1.2, 1.3, 1.5, and 1.6 that describe the effective medium constants for nanowire and multilayer structures, we notice that it is possible to have values of the permittivities of the constituent materials such that there will be poles or zeros in each equation. This is ideal to characterize the resonances of the metamaterials and from that, infer their hyperbolic behaviour. The effective medium constants are plotted for both a multilayer and nanowire metamaterial in figure 1.4(a) and (b), respectively. The multilayer metamaterial consists of alternating layers of silver and titanium dioxide with a metallic fill fraction of 35%. The nanowire structure simulated is an array of silver nanowires embedded in a aluminum oxide

(alumina) dielectric matrix with a metallic fill fraction of 15%. We note that figure 1.4(b) is for a silver nanowire structure in an alumina matrix. However, the main focus of this thesis is on the design, fabrication, and characterization of gold nanowire metamaterials. Figure 1.3(c) shows an Scanning Electron Microscopy (SEM) image of a silver/silica multilayer structure. Figure 1.3(d) shows an SEM image of a gold nanowire structure with the alumina matrix etched away to clearly show the gold nanowires. There are wavelength ranges shown where both Type I and Type II HMM behaviour are possible. Type I behaviour is shown in the nanowire structure over a wider wavelength range than the multilayer structure where it is easier to see Type II behaviour. The shaded regions on the plots in figure 1.4 [34]show the Type I and Type II behaviour for each structure. Type II behaviour is easier to see in multilayer structures because of the higher reflectance due to two components of the permittivity tensor being less than zero or metallic. Type I behaviour is more common in nanowire structures because of only one component of the tensor being metallic or negative.

Another striking difference between nanowire and multilayer structures is the direction of the Epsilon-Near-Zero (ENZ) and the Epsilon-Near-Pole (ENP) resonances. The ENZ is defined where the permittivity crosses zero in either the parallel or perpendicular direction while the ENP is where the permittivity approaches infinity due to the denominator of the permittivity relation approaching zero. The reflection and transmission spectra change drastically depending on the direction of these resonances. The ENZ occurs parallel to the thin film layers in the multilayer structure and parallel to the long axis of the nanowire in the nanowire metamaterial. This is intuitively satisfying as the Drude plasma frequency, which determines the ENZ of a material, is in the direction of free electron motion. It is highly sensitive to the metallic fill fraction of the metamaterial. The ENP occurs in the direction for which there is no free electron motion in the material. It occurs perpendicular to the thin film layers in the multilayer and perpendicular to the long axis of the nanowire structure. Figure 1.3 shows the direction of the ENP and ENZ in each structure. The effect of the ENZ, ENP, and hyperbolic behaviour on the propagating wave reflection and transmission spectra will be discussed in detail in chapter 2.

1.4 Fabrication and Characterization

There were a few different techniques used to fabricate the multilayer and nanowire metamaterials. Multilayer structures rely on the growth of ultra-smooth and ultra-thin films. Sputter Deposition was used to grow amorphous silicon, silicon dioxide, and tungsten films for the multilayer metamaterials. Titanium dioxide and gold were grown using electron beam evaporation. Surface roughness is an issue for many

practical applications of thin films and accumulates very quickly when many layers are being grown to form a multilayer structure. However, it has been shown that minor deviations in the layer thicknesses do not significantly change the effective medium response of the metamaterial [7]. Significant research is still being done to grow smoother thin films in order to improve the quality of the plasmonic resonances of the structure.

There is a standard procedure for growing 2D nanowire metamaterials [40, 41, 1]. It consists of growing metallic nanowires in alumina templates [41, 40]. Alumina templates can either be bought off the shelf or grown by oxidizing aluminum foil or aluminum thin films. Multiple groups have fabricated gold and silver nanowire structures using both of these methods [1, 37, 41, 21]. For this thesis, the template was grown by anodizing aluminum thin films. The process started with a 20nm thick titanium dioxide wetting layer being grown on a glass substrate via atomic layer deposition (ALD). A 7nm gold film is then sputtered on top to act as a cathode for the electrodeposition step of the growth process [41]. A 800nm film of aluminum is the last layer deposited via sputter deposition to form the template. A two step anodization process using 3% oxalic acid in an anodization cell to anodize the aluminum forms a porous structure that acts as a dielectric medium to support nanowire growth [41]. The concentration and type of acid controls the porosity or fill fraction of the alumina template used for nanowire growth. Finally, a multi-step electrodeposition process is used to grow silver or gold nanowires inside the alumina template. Electrodeposition is similar to electroplating in that an electrolyte containing ions of the metal to be deposited is used and voltages are applied to the substrate (gold cathode) and counter electrode (anode). The multi-step process ensures consistent filling of silver or gold across the entire template to increase quality of the ENZ and ENP resonances of the structure. Any overfilling of the template can be addressed after fabrication using ion milling. In addition, nanowire samples were annealed in a neutral gas atmosphere at 300^oC to improve the mean free path and overall quality of each gold wire.

Ellipsometry and Spectrophotometry were the two main methods used to characterize multilayer and nanowire metamaterials for work in this thesis. Ellipsometry and Spectrophotometry measure (p) and (s) polarized reflection and transmission across a broad spectrum of wavelengths and angles. Peaks or valleys across the reflection or transmission spectrum at specific wavelengths indicate the location of ENP or ENZ resonances.

1.5 Overview

The main challenge in this field involves taking metamaterials from the design stage to the fabrication and characterization stage. This thesis focuses on taking many different theoretical designs of nanostructures to the fabrication stage and characterizing their optical properties to match theoretical simulations.

Chapter 2 focuses on the simulation of gold and titanium dioxide nanowires. The structures simulated and fabricated were straight and inclined nanowires as well as helical nanowires using CST Microwave Studio software and Maxwell Garnet Effective Medium Theory to match experimental results. We show that in straight gold nanowires, there are two unique plasmonic resonances, both tunable to the type of material used. The ENZ resonance is tunable to the geometry of the nanowire structure. Inclined and helical nanowires were studied for applications in polarization manipulation in photonic circuits.

In chapter 3 we show theoretically that light can accumulate a non-dynamic Geometric Phase using the Jones matrix and Stokes parameters approach to represent the state of polarization of light over a closed path in both interferometry experiments and helically wound optical fibers. A new compact gold helical nanowire metamaterial is also proposed that can act as a circular polarizer, different from bulk polarizers seen in many of todays optical experiments.

Chapter 4 shows the first experimental proof of the recently proposed concept of relaxed total internal reflection for higher confinement of light inside the core of a waveguide for use in photonic circuits using a silicon/silica multilayer metamaterial as the cladding material deposited directly onto glass and silicon prisms.

Finally, in some future work, we show some initial CST microwave studio simulation results on thermal metamaterials to control light absorption and thermal radiation emission.

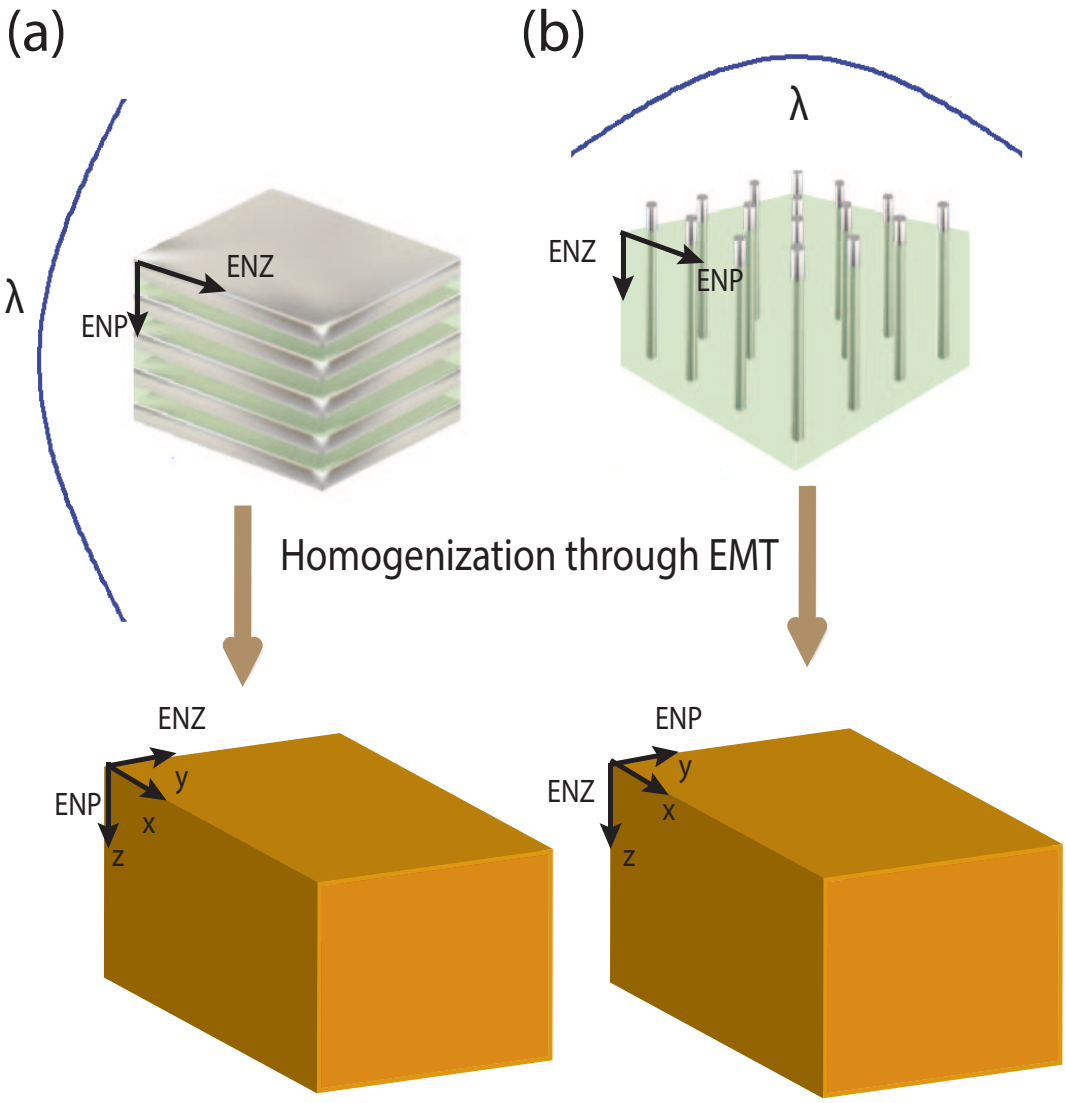

Figure 1.3: [34] (a) A multilayer HMM with ENP perpendicular to the interface and ENZ parallel to the interface can be homogenized to a bulk anisotropic material using Effective Medium Theory (EMT) as long as the layer thicknesses are much smaller than the wavelength of radiation. (b) A nanowire HMM with ENZ perpendicular to the air/material interface and ENP parallel to the interface can be homogenized to bulk anisotropic material using EMT with wire radius and interwire spacing much less than the wavelength of radiation.

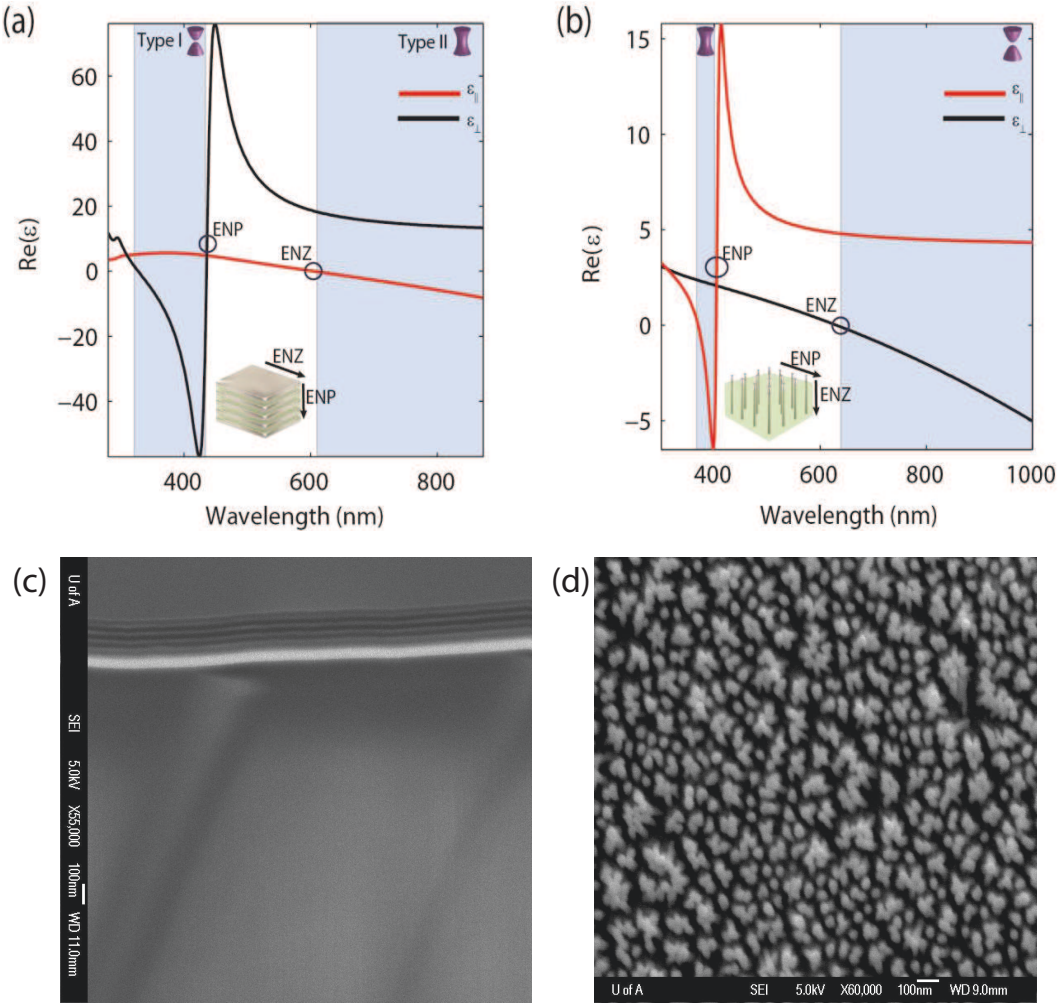

Figure 1.4: [34] Real part of the dielectric constant vs wavelength for a gold/titanium dioxide multilayer structure with 35% fill fraction (a) and a silver/alumina nanowire structure with 15% fill fraction (b). Scanning Electron Microscopy Images (SEM) of a silver/silica multilayer structure (c) and gold nanowire structure (d). Insets show schematics of the structures simulated.

Chapter 2

Straight, Inclined, and Helical Nanowires

Nanowires are a type of nanostructure that is becoming increasingly common for applications in sensing [43] and nanowaveguiding [13]. Advancements in fabrication are making the growth of nanowire structures simpler and faster with a wider range of materials. For this thesis, we focus on the optical properties of straight, inclined, and helical gold and titanium dioxide (TiO2) nanowire structures.

2.1 Straight Gold Nanowires

As a 2D HMM, nanowire arrays have special optical properties. These optical properties are most easily measured by examining the propagating wave reflection and transmission spectra. Hyperbolic behaviour can only be observed with (p) polarized light, so for our study we examine both (p) and (s) polarized light and contrast the differences. This is apparent because in order to access free electron motion along the z axis (long axis of the nanowire) a component of the incident electric field has to lie in the same direction as free electron motion in order to excite free electrons in the ENZ response of the metamaterial. In the nanowire structure, the ENP and ENZ resonances interact with propagating waves and can lead to large absorption or optical density. For this thesis, optical density (OD) or extinction is defined as

$$OD = -log(T) \tag{2.1}$$

where T is defined as the power transmitted through the nanowire structure. Near the ENZ, we expect very large absorption. Very large absorption is the result of very large electric field magnitudes inside the structure. If we examine the boundary condition, $\epsilon_0 E_{0\perp} = \epsilon_{1\perp} E_{1\perp}$, we see that when $\epsilon_\perp \to 0$ the electric field magnitude must become incredibly large inside the structure for the condition to hold. The

ENZ resonance only occurs for (p) polarized light and is highly sensitive to the metal filling fraction. The ENZ makes the nanowire structure ideal for sensing applications [20, 43].

The ENP resonance is only weakly dependent on fill fraction. This is because the parallel part of the permittivity tensor interacts with both (p) and (s) polarized light as the electric field for both (p) and (s) polarized light has a component that lies in the parallel plane of the nanowire structure. In literature, the ENP is often referred to as the Transverse (T) resonance and the ENZ as the Longitudinal (L) resonance.

Simulations for a straight gold nanowire structure were performed using both EMT and CST Microwave Studios software with a metal fill fraction of 22% and wire length of 700nm. The computation was performed over the wavelength range 300nm to 1000nm at normal incidence, 40^o, and 60^o. The two absorption peaks seen in figure 2.1(a) for (p) polarized light correspond to the T resonance or ENP and the L resonance or ENZ. In figure 2.1(b) we only see the T resonance as (s) polarized light was used to excite the structure in this example. Beyond the ENZ wavelength, $\epsilon_\perp$ becomes negative and the nanowire structure exhibits Type I behaviour.

The T resonance does not change with angle and occurs for both (p) and (s) polarizations at a wavelength of approximately 530nm. A slight discrepancy occurs in the magnitude of the T resonance between EMT and CST due to the discrepancy between the dielectric permittivity used for each method along with the difference in computation algorithm. We emphasize that the main outcome is the resonance occurring in the same location for both methods.

The L resonance for this structure occurs at 602nm and is only seen for (p) polarized light as explained earlier. The magnitude of the resonance increases drastically with increasing angle and is not seen at normal incidence. This occurs because at normal incidence, the direction of the electric field vector lies entirely in the plane perpendicular to the axis of the wire. However, as the angle of incident (p) polarized light increases, a component of the electric field vector grows along the direction for free electron motion along the long axis of the wire. The greater the magnitude of the fields along this axis, the greater the magnitude of the resonance. The quality of the resonances is dependent on the quality of the electrolyte solution used to grow gold nanowires embedded in the alumina. A modified model from [38] was used to more accurately describe the permittivity for gold for very small structures where the mean free path of electrons is restricted.

A striking difference exists at higher angles for simulations performed between CST and EMT. For the CST simulation at large incident angles, there is a shift of the L resonance to shorter wavelengths. This has been examined in previous papers and can be attributed to non-locality and material loss [38]. Non-locality

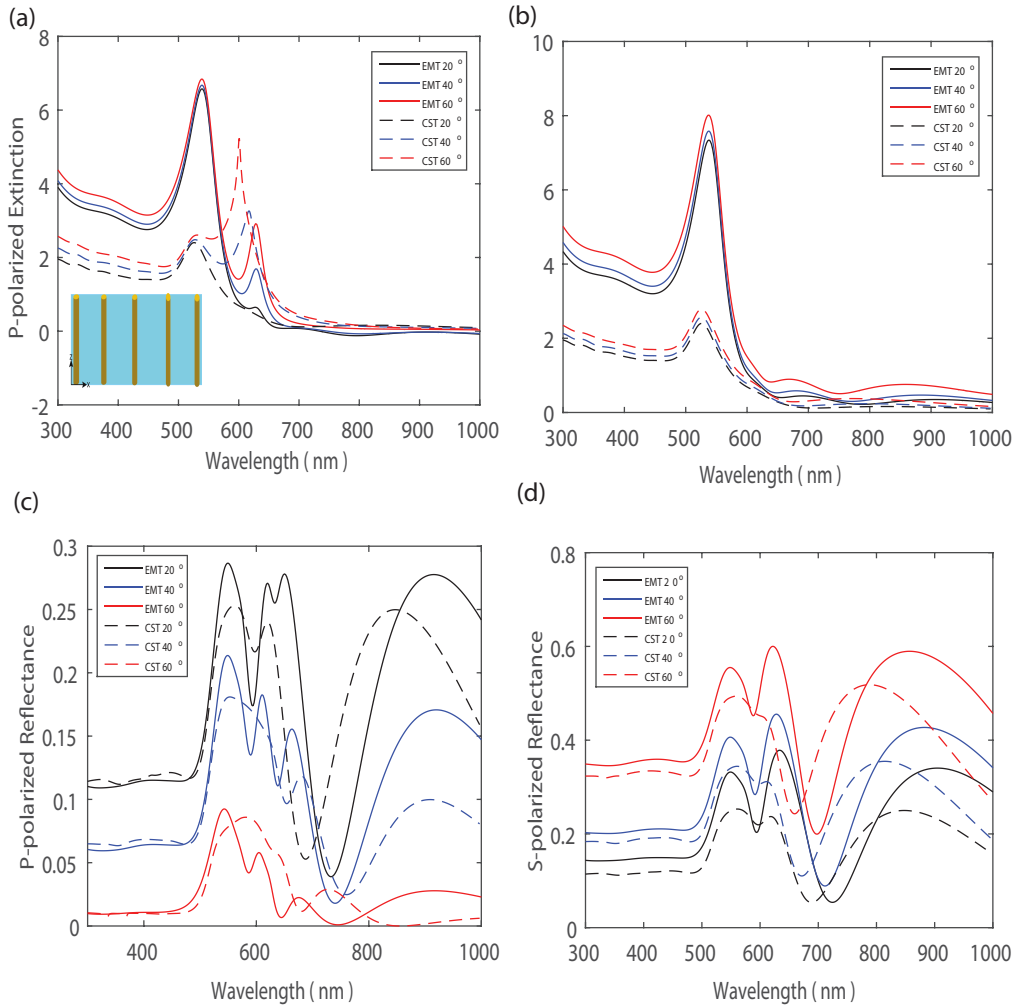

Figure 2.1: Extinction for (p) polarized (a) and (s) polarized (b) light through a straight gold nanowire structure with wire length of 700nm and a fill fraction of 22% using both EMT and CST Microwave Studios simulation software. Reflectance for (p) polarized (c) and (s) polarized (d) light through a straight gold nanowire structure using both EMT and CST Microwave Studios simulation software. An excellent agreement is seen between the analytical model and numerical simulation.

occurs due to spatial dispersion in metamaterials from variations in the fields on the scale of material inhomogeneity. That is to say, the fields will be altered by the response from surrounding unit cells, hence the name non-locality. The reason we see the effect of non-locality in CST and not EMT, is because near the L-resonance, the response becomes wave vector dependent. Conventional EMT theory can not account for this and an additional spatial dispersion term has to be added to the effective medium picture [38].

The reflection spectrum for (p) and (s) polarized light for our nanowire structure is shown in figures 2.1(c) and 2.1(d), respectively. The three reflection peaks seen for all angles and both polarizations are Fabry Perot resonances that occur from thin film interference due to the change in location of reflection peaks for differing incident angles. A second detail to observe from the reflection spectrum is the existence of a Brewster Angle. This is evident as for (p) polarized light, the magnitude of reflectance approaches zero as the angle of incident gets higher and reaches its lowest point at 60^o at wavelengths longer than the L resonance. This confirms what is predicted from theory that the nanowire structure is a Type 1 HMM at wavelengths longer than the L resonance. The reflection spectrum can also be used to experimentally determine the quality of our samples based on diffuse scattering measurements. A higher magnitude of reflection indicates that diffuse scattering effects are limited for the particular sample and the wires are high quality.

Gold nanowire metamaterials were fabricated as explained in section 1.4 on rigid BK7 glass substrates with various filling fractions. In order to change the fill fraction of our samples, the wire diameter had to be varied which was done immediately after the anodization stage by using a wet etch with 5% concentration phosphoric acid to widen the pore diameters in the porous alumina film.

Angularly resolved transmission spectroscopy was used to measure the extinction spectrum for various gold nanowire samples ranging from fill fractions of 10.5% to 26% using the experimental setup shown in figure 2.2(a). The spectra are measured using an Ocean Optics fiber optic spectrometer and linearly polarized white light from an incandescent light bulb coupled through a collimated optical fiber. A lens was used to focus the incident light to a spot size of 0.5mm on our nanowire sample. A second lens was used to focus the output transmitted spectrum into another optical fiber coupled to the spectrometer. Figures 2.2(b)-(d) shows the extinction spectrum for samples with fill fraction of 26% (b), 23% (c), and 10.5% (d). Fill fractions were measured post processing as the samples had to be cleaved to take images. A scanning electron microscopy (SEM) image was taken for each of the 3 samples. The image was then run through a code that outputs the ratio of "dark" pixels to "light" pixels. "Dark" pixels were attributed to the pores as they had a contrast below the boundary for electron detection to show up on the image while

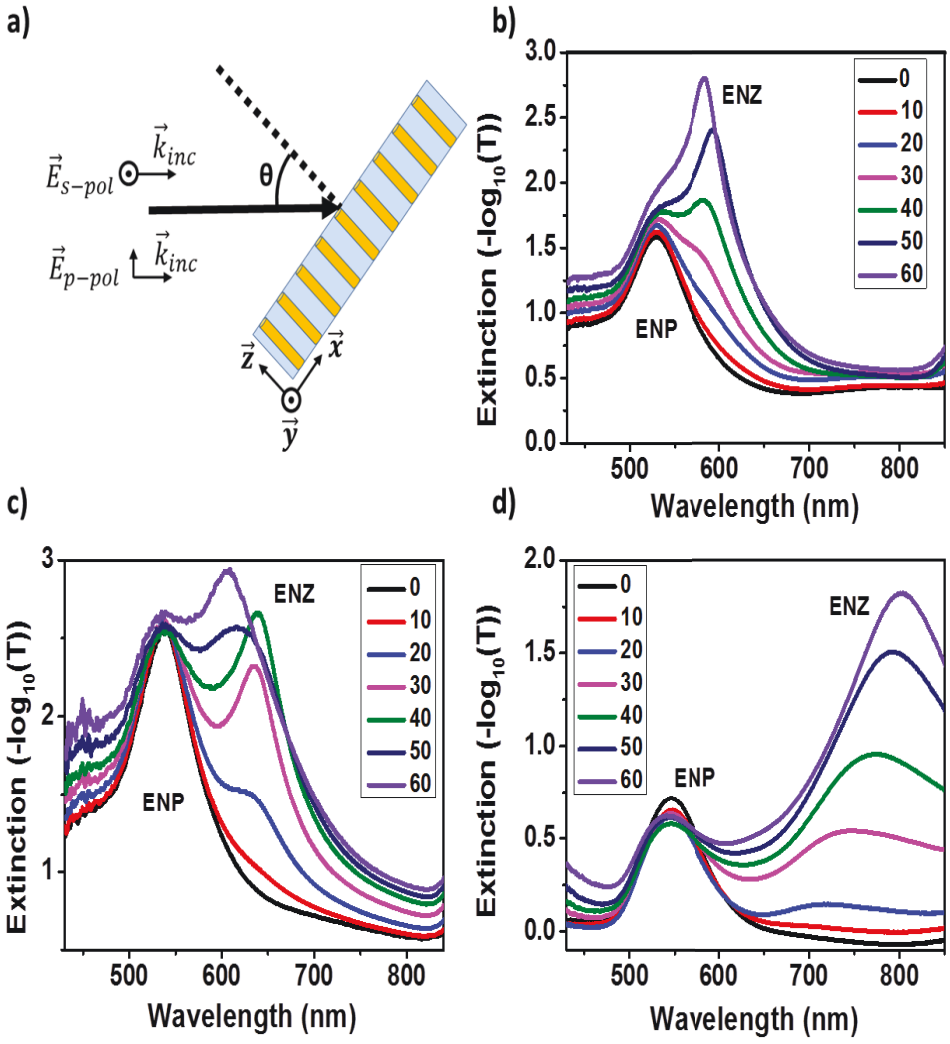

Figure 2.2: [41] (a) Experimental Setup for measurement of extinction (-log10(T)) for a gold nanowire structure. Experimental Extinction measurements a for gold/alumina nanowire structure using fill fractions of 26% (b), 23% (c), and 10.5% (d).

"light" pixels represented the alumina matrix with contrast above the minimum threshold for detection of scattered electrons in the image.

The first absorption peak is located at $530 \pm 10nm$ for all samples as expected and corresponds to the ENP resonance. It's location is generally only dependent on the materials used to form the nanowire structure for fill fractions much less than 100%. The ENP is present for both (p) and (s) polarized light and the magnitude of the resonance does not increase or decrease with incident angle of light.

The second absorption peak corresponds to the ENZ and only occurs when p-polarized light is used for excitation. The ENZ occurs due to free electron motion

along the long axis of the nanowire. As the angle of incidence increases, so does the magnitude of the ENZ peak from the growing magnitude of the electric field vector parallel to the nanowire long axis. This resonance can be tuned by adjusting the fill fraction from 583nm for a fill fraction of 26% to 805nm at a fill fraction of 10.5%. Beyond the ENZ resonance, the perpendicular permittivity component of the dielectric tensor is negative and the sample is hyperbolic Type I. The ENZ resonance blue shifts at higher incident angles due to the effect of non-locality and material loss explained previously [38].

Diffuse scattering is a major source of uncertainty for extinction measurements. It can be difficult to accurately determine exactly what fraction of the power is being absorbed inside the nanowire metamaterial at the ENP and ENZ resonances. We plotted the ratio of T_p/T_s to study the scattering effects from our samples. The scattering effects should be canceled out in this ratio as scattering will be the same for both (p) and (s) polarized light. Figure 2.3(a) shows good agreement between CST and experiment indicating that our samples do not suffer from significant scattering effects.

The experimentally determined locations of the ENZ and ENP are plotted in figure 2.3(b) vs fill fraction along with the theoretical curves calculated from EMT for a nanowire structure explained in section 1.3 for ENZ and ENP locations for all fill fractions from 10% to 30%. The ENP resonances are weakly dependent on the fill fraction of the nanowire metamaterial and are purely from plasmonic resonances. No peaks exist in the extinction spectrum from Fabry-Perot resonances for our nanowire samples. It was stated earlier that this was only true when $\rho << 1$, however, we observe it holds true for larger values of ρ shown here. The experimental ENZ points for each fill fraction agree well with the theoretical curve in this case. The shift at higher incident angles from non-local effects or spatial dispersion is more evident here as shown in the change in ENZ with incident angle by the varying size of the data points in figure 2.3(b).

It has been demonstrated that highly tunable gold nanowire metamaterials can be easily fabricated and characterized. Future experimental work with these samples will explore biosensing [43, 20], quantum [45, 29, 19], and thermal applications [39].

2.2 Inclined Gold Nanowires

A second type of gold nanowire metamaterial designed in this work is the inclined gold nanowire structure. This involves the tilting of the nanowires from vertical to an inclined angle either in the vertical (out-of-plane) or horizontal (in-plane) direction [17]. Tilting the nanowires creates a higher degree of anisotropy compared to vertical nanowires and can be used for applications in polarization conversion [6]. This is

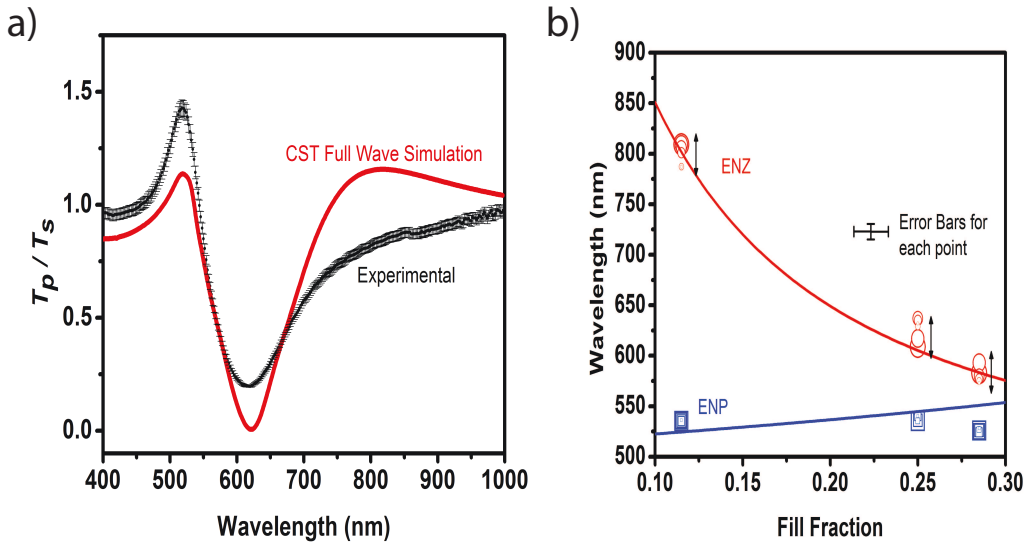

Figure 2.3: [41] (a) (p) polarized transmittance divided by (s) polarized transmittance for a straight gold nanowire sample at an incident angle of 30^o for a sample with fill fraction 26%. Both experimental results and CST simulations show no diffuse scattering from the nanowire samples. (b) The location of the ENP and ENZ experiment vs fill fraction. The ENP stays at roughly the same location (530nm) for all fill fractions while the ENZ is highly tunable from 583nm at $\rho = 26\%$ to 805nm at $\rho = 10.5\%$.

important as manipulation of the shape and phase of light is required in various applications. Most polarizers are bulky and can not be integrated into photonic circuits. On chip analyzers are important for the realization of photonic circuits. The design requirement of this study was to find an anisotropic metamaterial that could convert incident polarized light from (p) to (s) or (s) to (p) polarization at an efficency of 100% over a tunable wavelength range.

With the tilting of nanowires for polarization conversion, it becomes apparent that the traditional Fresnel equations and transfer matrix method for transmission and reflection are not enough to fully describe the anisotropy of the tilted nanowire structure. A 4x4 anisotropic transfer matrix method has been derived in detail in [16] and can be used to predict the conversion of (p) to (s) or (s) to (p) polarization upon reflection from or transmission through the interface of an anisotropic metamaterial. These variables are referred to as R_{ps} for conversion of (p) polarized light to (s) polarized light while the opposite is true for R_{sp}. The same syntax applies for transmittance as T_{ps} represents conversion of (p) to (s) polarized light for light transmitted through the metamaterial while T_{sp} is for the opposite case.

The first structure designed uses gold nanowires tilted vertically at an angle of

40^o measured from the surface normal vector of the metamaterial. The structure has a wire radius of 16nm, inter wire spacing of 65nm, 300nm length, and is embedded in an alumina matrix. This gives a filling fraction of 22%. The wire length is defined as the thickness of the homogenized metamaterial. A schematic is shown in the inset of figure 2.4(d). Gold is chosen as the material here to try and take advantage of the ENZ that occurs in the visible region. Polarization conversion is more likely to occur near the ENZ due to accumulation of phase for some polarizations but not others. This is ideal to add an arbitrary phase to manipulate the polarization state of light. The region of interest for this particular case is from 300nm to 1000nm. Simulations were done using CST Microwave Studios to calculate the reflection and transmission coefficients of the structure.

Isotropic reflection is where light remains in the same state of polarization for (p) and (s) polarized light. Reflectance from our structure is shown at normal incidence, 40^o, and 60^o in figure 2.4(a) while the anisotropic case is shown in figure 2.4(b). Anisotropic reflection occurs when the state of polarization is changed from (p) to (s) or (s) to (p) polarizaiton upon reflection or transmission through a material. The reflection peaks in the isotropic case are Fabry Perot resonances as the location of the peaks change with change in incident angle. The anisotropic reflection in figure 2.4(b) show a small fraction (5-15%) of light is converted from (p) to (s) polarization and vice versa. This is not ideal for a polarizer as it will mix (p) and (s) polarized light and it won't meet our requirement of 100% polarization conversion efficency.

The isotropic transmittance (figure 2.4(c)) shows high transmittance through the sample. The anisotropic transmittance (figure 2.4(d)) shows a higher fraction of light being converted from (p) to (s) and (s) to (p) polarized radiation (max of approximately 55% at 900nm), however it still does not meet the requirement of the design when the sample is used in transmission mode.

The vertically inclined gold nanowire sample can be rotated 90^o about the surface normal vector so that the nanowires are tilted in the plane of incidence or horizontally in order for the wires to become coplanar with the incident electric field. This allows the long axis of the wire to be in the same plane as the electric field vector for (p) polarized light to excite the ENZ resonance. The simulated transmission and reflection measurements for the isotropic case are shown in figure 2.5(a) and 2.5(c) and the anisotropic case in figure 2.5(b) and (d). There is an ENZ resonance that only occurs for (p) polarized light in the transmission spectrum at approximately 890nm. This is because the wires are tiled at an angle of 40^o so the angle of incidence has to be larger than normal incidence for a component of the electric field vector to be along the wire axis. This resonance also shows up in the anisotropic spectrum and can be used to convert (s) to (p) polarized light with 100% efficiency at an incident angle of 40^o. The conversion of (p) to (s) and (s) to (p) polarized light

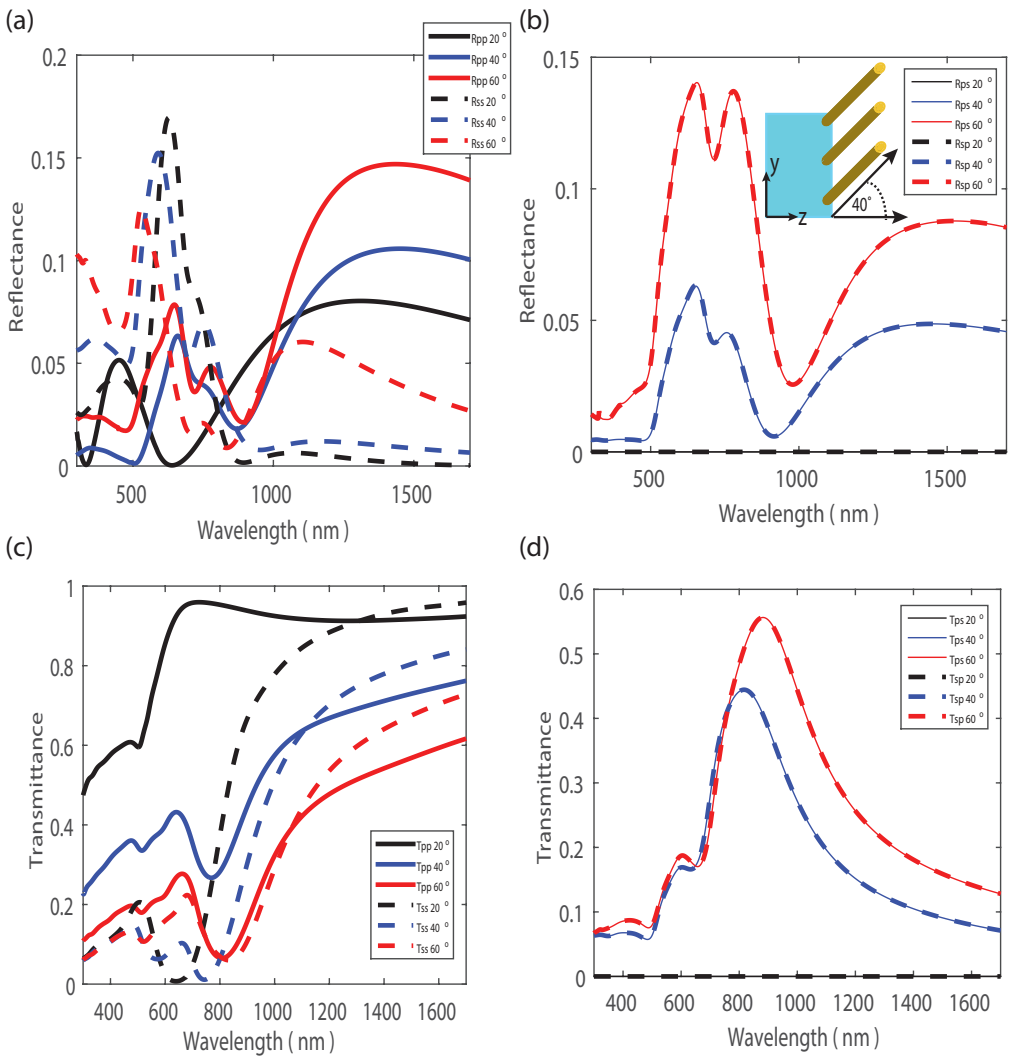

Figure 2.4: Isotropic (a) and anisotropic (b) reflectance of an out-of-plane vertically inclined gold nanowire metamaterial. The wires are tilted at an angle of 40^0, have a fill fraction of 22%, and the metamaterial slab is 300nm long. (c) and (d) show the isotropic and anisotropic transmittance of the same inclined nanowire structure. Inset in (b) shows a schematic of the structure.

comes from the phase accumulation for certain polarizations at certain wavelengths. This is most likely to occur near the polarization sensitive ENZ wavelength of the inclined nanowire structure [32].

2.3 Straight TiO2 Nanowires

TiO2 is another material we considered to use to study the optical properties of nanowire structures. TiO2 is chosen because of the low loss in the visible and near

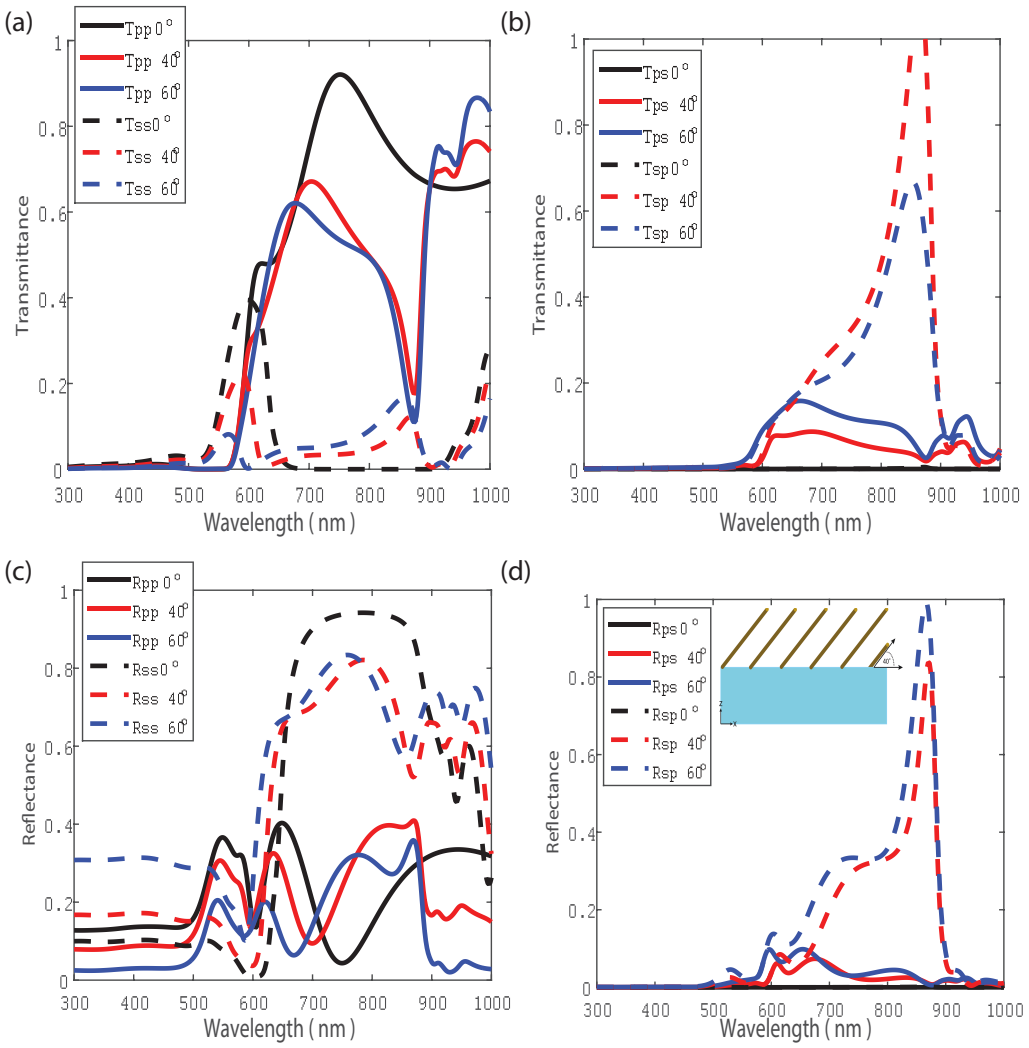

Figure 2.5: Isotropic (a) and anisotropic (b) reflectance of an in-plane horizontally inclined gold nanowire metamaterial. The wires are tilted at an angle of 40^0, have a fill fraction of 22%, and the metamaterial slab is 300nm long. (c) and (d) show the isotropic and anisotropic transmittance of the same inclined nanowire structure. Inset in (d) shows a schematic of the structure.

infrared region. Simulations are performed using EMT and TMM. The reflectance spectrum for (p) and (s) polarized light is shown in figure 2.6(a). There are no interesting features in the anisotropic reflectance. The wire radius is 16nm with wire to wire spacing of 65nm. The length of the wires is 300nm and the wires are surrounded by air. A sample was fabricated in collaboration with the Dr. Mike Brett research group [26] at the University of Alberta with approximately the parameters predicted in simulation.

The resulting reflectance spectrum is measured using ellipsometry and plotted

in figure 2.6(b). The reflectance spectrum from experiment matches what is seen in simulations with a reflectance peak corresponding to an atomic resonance in TiO2 at approximately 330nm as predicted from the material dispersion.

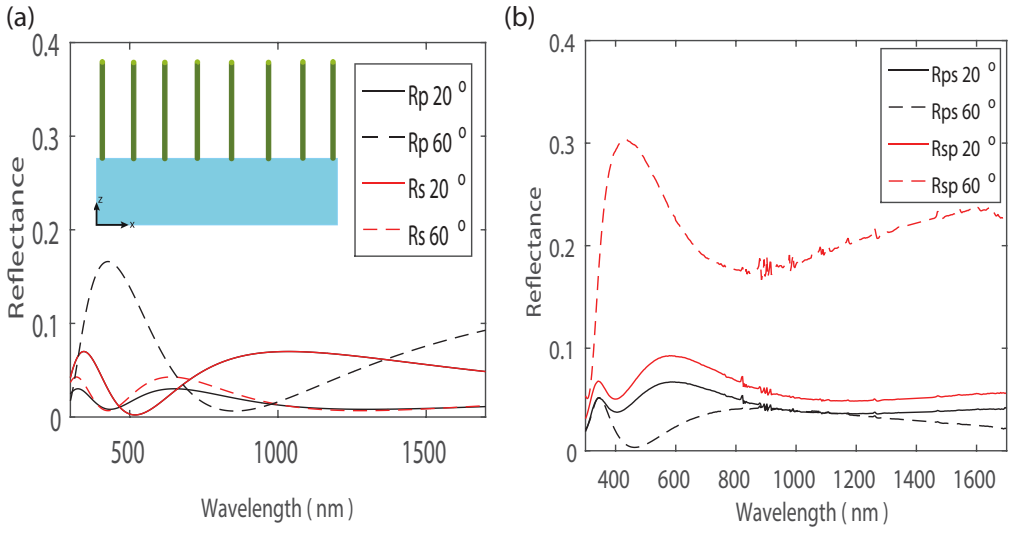

Figure 2.6: Comparison of theory (a) and experiment (b) for a straight TiO2 nanowire structure surrounded by air, with wire radius 16nm, wire to wire spacing 65nm, and length 300nm. The minor discrepancy can be related to the larger index of TiO2 in the fabricated sample.

2.4 Inclined TiO2 Nanowires

A higher degree of anisotropy can be created in TiO2 nanowires by tilting them horizontally or vertically, similar to the gold nanowires. The first structure studied has the TiO2 wires tilted vertically with the same length and fill fraction as the straight TiO2 nanowires. Simulations were performed using CST (vertically tilted wires) and EMT 4x4 anisotropic TMM method (horizontally tilted wires).

The reflectance spectrum for vertically tilted nanowires is shown in figure 2.7(a). The reflectance peaks that exist are purely Fabry Perot modes as the peak location changes with changing incidence angle. The anisotropic reflectance is plotted in figure 2.7(c). Only a maximum of 5% of the reflected light is expected to go from (p) to (s) or (s) to (p) polarization.

Tilted TiO2 nanowire samples were fabricated in collaboration with the Dr. Mike Brett Research Group [26] at the University of Alberta with wire radius 16nm, wire to wire spacing of 65nm, and length of 300nm using the Glancing Angle Deposition (GLAD) technique. This involves tilting the substrates to very large angles during deposition to grow tilted or helical structures [26]. The large angle of the substrate is

required so that the wires will grow at an angle and not normal to the interface of the substrate [26]. The isotropic and anisotropic reflectance spectra are measured using ellipsometry and are found to match what was predicted by theory in magnitude and locations of peaks as shown in figure 2.7(b) and 2.7(d).

This sample did not meet our design requirement because of the low polarization conversion efficiency so we repeated the simulations and characterization measurements with the same sample rotated by 90^o so that the nanowires were now tilted horizontally to lie in the same plane as the electric field vector for (p) polarized light. The simulations for isotropic reflectance are shown in figure 2.8(a) with the experimentally characterized reflectance in figure 2.8(b). Fabry-Perot resonances exist due to the change in reflection peak with incident angle for each sample with relatively low reflectance as expected for a TiO2 structure. The anisotropic reflectance is shown for the simulations in figure 2.8(c). Experimental measurements for anisotropic reflectance for this sample aren't shown as they showed no conversion upon reflection at the air/metamaterial interface of (p) to (s) or (s) to (p) polarized light. The degree of polarization conversion is very low and we conclude the design for polarization conversion using TiO2 did not meet our design requirement. Other materials with plasmonic or polariton resonances in the region of interest would be a better candidate to meet our goal as polarization conversion occurs at a high efficiency near plasmonic/polaritonic resonances.

2.5 Helical TiO2 Nanowires

TiO2 helical nanowires can be fabricated via the GLAD technique [26] and the structure is shown in figure 2.9(a). Helical structures require continuous rotation of the substrate during deposition to form the helix pattern [26]. The simulated structure had a wire radius of 5nm, helix radius of 50nm, and wire length of 500nm. The wire length is defined as the thickness of the homogenized helical nanowire structure. The helical wires were grown in vacuum on a glass substrate. Air is the surrounding medium of the wires. This structure was designed to study circularly polarized light in the mid infrared region of the electromagnetic spectrum. Figure 2.9(b) shows the transmittance of left handed circularly polarized light (LCP) and right handed circularly polarized light (RCP) simulated using CST Microwave Studios. From the transmission spectrum we can infer that helical TiO2 wires will not work as a circular polarizer as the transmittance of LCP and RCP through the metamaterial is approximately the same. In order to work as a circular polarizer, a material has to absorb one circular polarization and transmitor reflect the other. We will see how to optimize the difference between LCP and RCP absorption in the next chapter.

Straight, inclined, and helical nanowires have been designed and simulated for

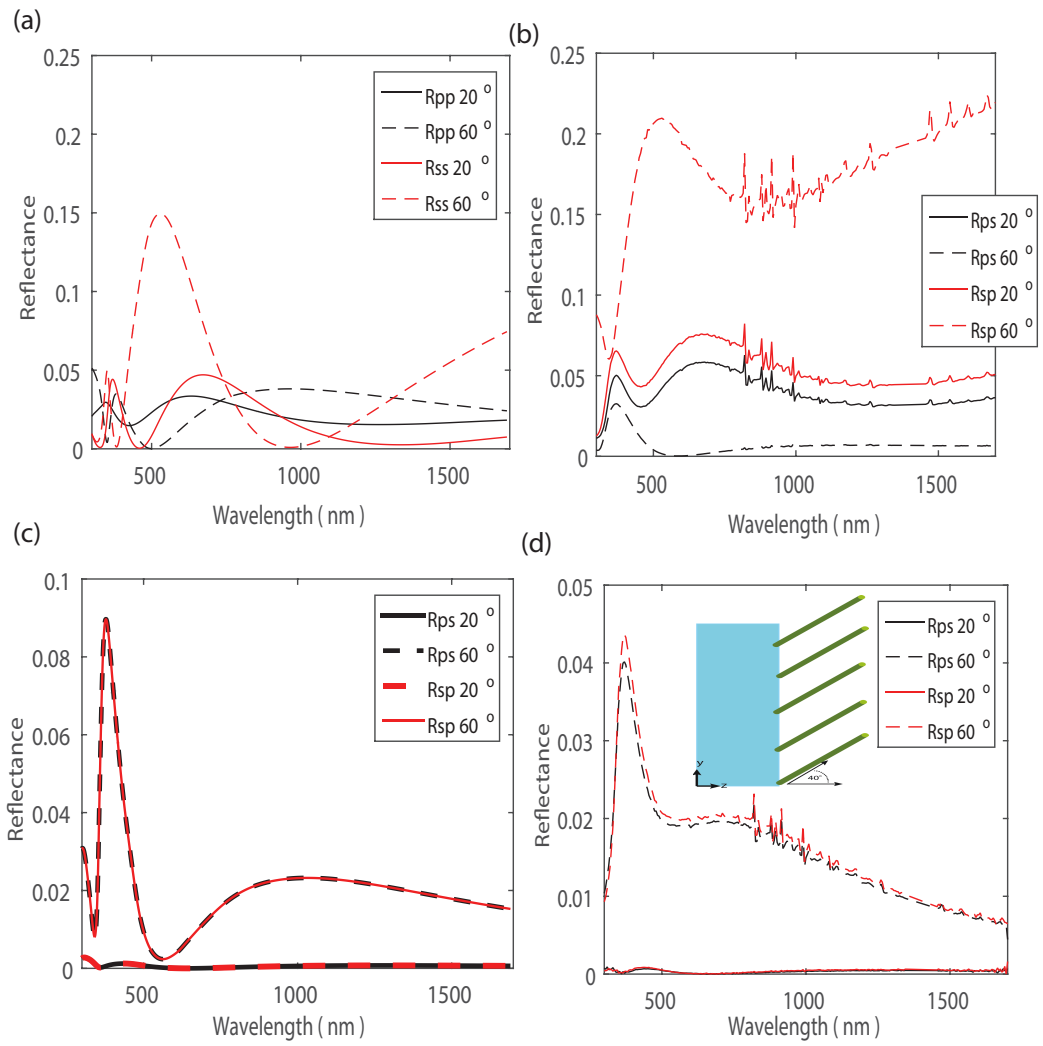

Figure 2.7: Theoretical CST simulations (a) and experimental measurements (b) for the isotropic reflectance of vertically inclined TiO2 nanowires surrounded by air. Anisotropic reflectance simulated using CST microvwave studios (c) and experimental results (d) for conversion of (p) to (s) and (s) to (p) polarization. The radius of the wire is 16nm and the wire to wire spacing is 65nm. The thickness of the metamaterial slab is 300nm.

polarization conversion for photonic circuits. They are simulated, fabricated and characterized with horizontally tilted in-plane gold nanowires showing the best results to the design requirement of completely converting (p) to (s) or (s) to (p) polarized light near the ENZ wavelength. The next design step is to make the operating bandwidth of polarization conversion wider or find other materials to grow nanowires that rotate polarization by a controlled amount at 100% conversion efficiency in other regions of the electromagnetic spectrum.

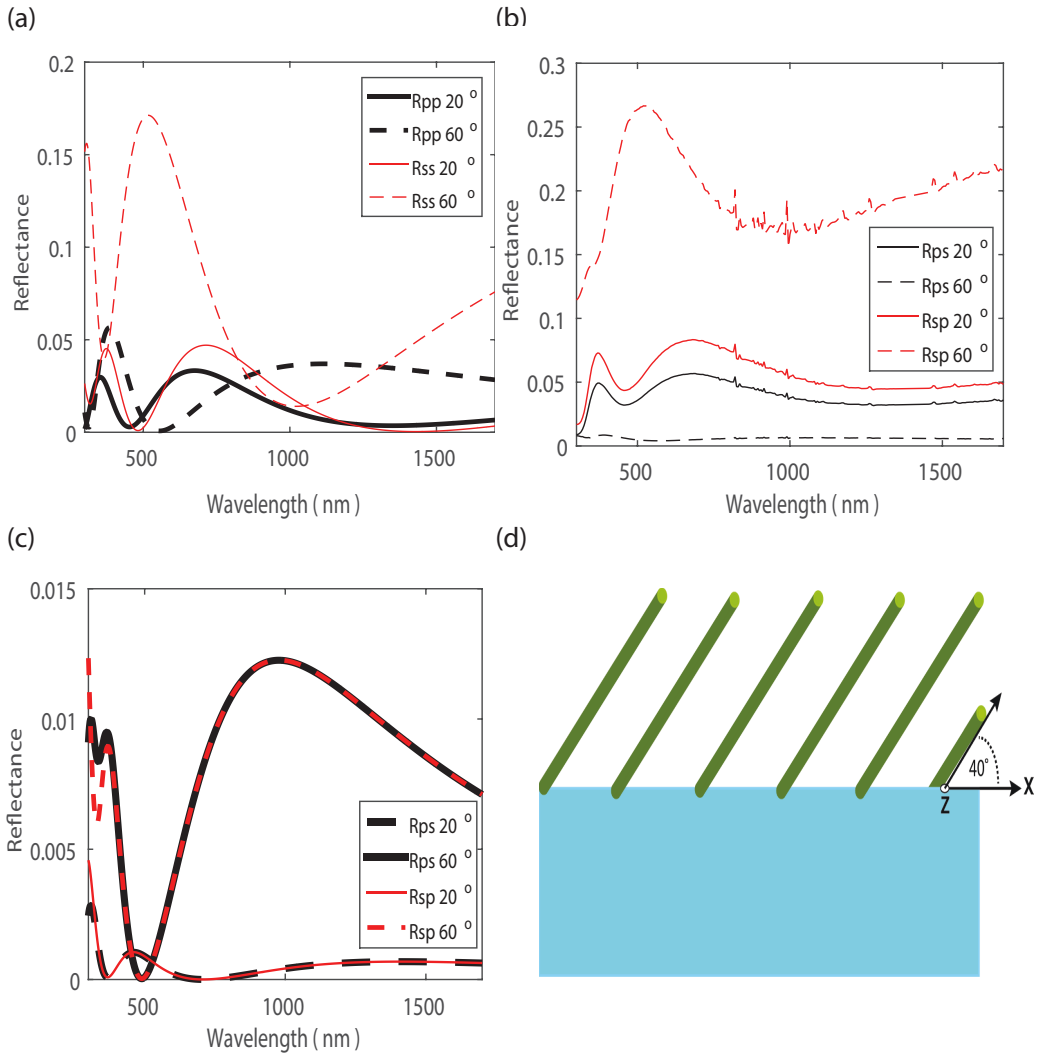

Figure 2.8: p and s-polarized reflectance calculated using EMT (a) and experimental measurements (b) of a TiO2 inclined nanowire structure with the wires tilted horizontally in-plane. Anisotropic reflectance simulated using CST microvwave studios (c) for conversion of (p) to (s) and (s) to (p) polarization. (d) Schematic of the in-plane horizontal inclined TiO2 nanowires. The fill fraction of the wire structure surrounded by air is 22% and the thickness of the metamaterial slab is 300nm.

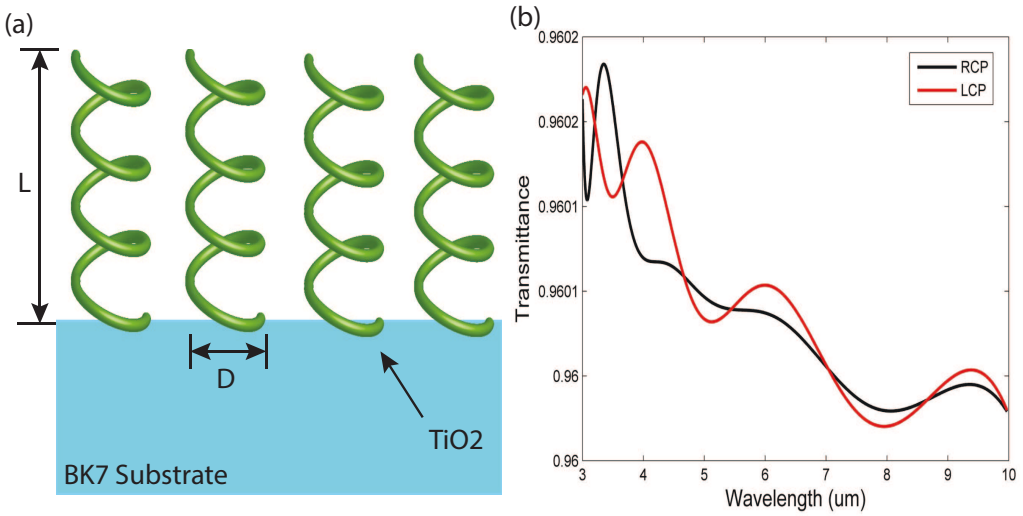

Figure 2.9: (a) Schematic of helical TiO2 Nanowire Structure surrounded by air grown on a BK7 glass substrate with wire radius of 5nm, helix diameter, D of 100nm, and length, L of 500nm. The TiO2 helix is surrounded by air on a glass substrate. (b) Transmittance of Left Circularly Polarized Light (LCP) and Right Circularly Polarized Light (RCP) through the Helical Nanowire.

Chapter 3

Geometric Phase in Photonic Nanostructures

Modern photonic components that alter the phase or polarization of light are large, bulky, and can not be integrated into photonic circuits easily [10, 46]. With the advancements of nanofabrication and the drastic decrease in size of circuit elements over the last decade, this has become a major problem. Birefringent crystals are commonly used as rotators of polarization but are very expensive and bulky. A new type of device must be designed in order to manipulate beams of light for photonic circuits.

Geometric phase is a type of adiabatic phase that occurs when light travels around a closed path on the Poincaré Sphere or in Momentum space. Meta surfaces and metamaterials that alter the phase of light have recently been proposed as on chip polarizers, analyzers, and diffraction elements [10, 18, 46]. Geometric phase can be used to order to alter the polarization state of the light without the use of bulky and expensive crystals.

3.1 The Poincaré Sphere

The Poincaré Sphere is a convenient way to represent the polarization state of light and show how the polarization state of light changes as it travels along a path through different optical components in an optical experiment [2]. It is represented by a sphere shown in figure 3.1(a). There are four parameters or components of the Stokes Vector used to represent the polarization state of light. The Stokes Vector is a 1x4 vector with components S_o, S_1, S_2, and S_3 [2]. S_o represents the radius of the sphere or the intensity of the light. S_o is always a positive quality and defined as

$$S_o = E_x E_x^* + E_y E_y^* \tag{3.1}$$

where E_x is the component of the field polarized on the $\overrightarrow{x}$ axis and E_y the field polarized along the $\overrightarrow{y}$ axis. It is most commonly normalized to a value of 1 for convenience [2].

S_1 represents the state of lineally polarized light and is defined as

$$S_1 = E_x E_x^* - E_y E_y^* \tag{3.2}$$

If $S_1 < 0$ the light is linearly polarized more towards the $\overrightarrow{y}$ direction and $S_1 > 0$ if the light beam is polarized toward the $\overrightarrow{x}$ direction. The limits of ± 1 represent completely $\overrightarrow{y}$ polarized light for -1 and completely $\overrightarrow{x}$ polarized light for +1 [2].

S_2 represents the relative light intensity that is polarized at either -45^o or $+45^o$. It is defined as

$$S_2 = E_{45} E_{45}^* - E_{-45} E_{-45}^* \tag{3.3}$$

where E_{45} and E_{-45} are found by a simple transformation of coordinate systems from the $\overrightarrow{x}$-$\overrightarrow{y}$ plane to the $\overrightarrow{x}' - \overrightarrow{y}'$ plane rotated by 45^o as measured from the $\overrightarrow{x}$ axis [2]. If $S_2 = +1$, the light is completely polarized at $+45^o$ and -1 for -45^o [2].

Lastly, S_3 represents the relative intensity of circularly polarized light [2]. It can be defined as

$$S_3 = E_{RCP} E_{RCP}^* - E_{LCP} E_{LCP}^* \tag{3.4}$$

where E_{RCP} and E_{LCP} represent the electric field for right and left circularly polarized light respectively [2]. They can be found by using the coordinate transformation

$$\begin{bmatrix} E_{LCP} \\ E_{RCP} \end{bmatrix} = \frac{1}{\sqrt{2}} \begin{bmatrix} 1 & i \\ 1 & -i \end{bmatrix} \begin{bmatrix} E_x \\ E_y \end{bmatrix} \tag{3.5}$$

This coordinate transformation comes from combining the Jones Vectors for LCP $(E_x + iE_y)$ and RCP $((E_x + iE_y)$. When $S_3 = 1$, the light is completely RCP and if it is -1, completely LCP.

The Mueller matrix is a 4x4 matrix that represents the effect an optical element or material has on the polarization state of light [2]. There are standard matrices in optics books for basic optical elements such as polarizers or wave plates [2]. More complicated metamaterials can have their Mueller matrix measured directly at each wavelength using ellipsometry.

On the Poincaré Sphere (figure 3.1(a)), S_1 is the $\overrightarrow{y}$ axis, S_2 is the $\overrightarrow{x}$ axis, and S_3 is the $\overrightarrow{z}$ axis [2]. A small point anywhere on the Poincaré Sphere represents completely polarized light while the whole sphere being highlighted means the light is completely unpolarized [2]. If the light beam has more than one of the Stokes Parameters non-zero, it can be either linearly polarized at some arbitrary angle (S_1

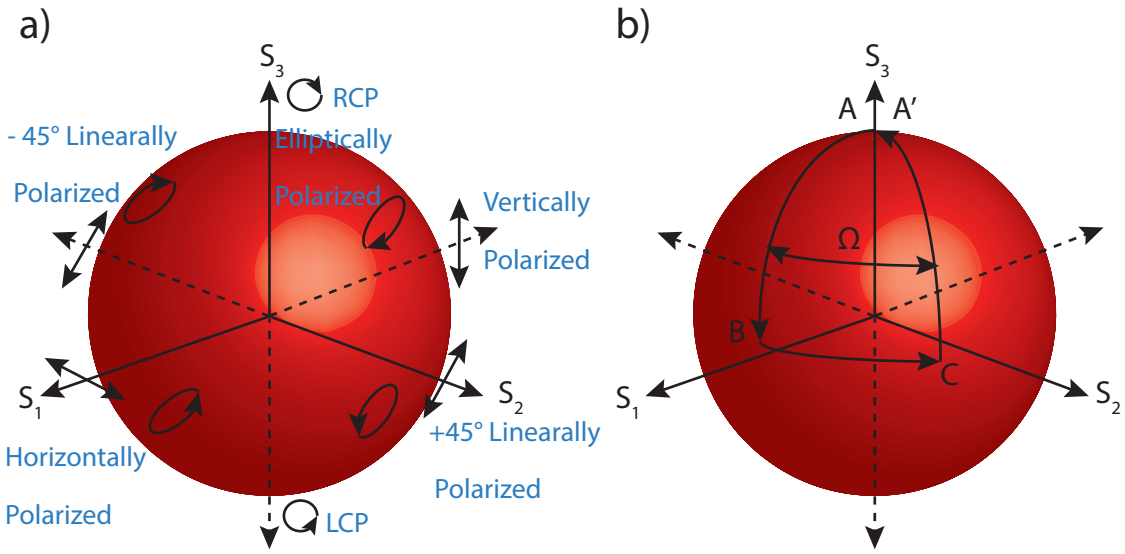

Figure 3.1: The Poincaré Sphere used to represent the polarization state of light. The North and South Poles represent right and left circularly polarized light respectively while the x - y plane represents linear polarization. (b) If light travels along a closed path along the Poincaré Sphere starting at one polarization and returning to the original polarization state through two intermediate states (B and C), it will acquire a phase difference equal to half the solid angle formed by the path traveled on the Poincaré Sphere.

and S_2 are non-zero) or elliptically polarized (S_1, S_2, and S_3 are non-zero) as shown in figure 3.1(a) [2].

Shivaramakrishnan Pancharatnam, in a paper published in 1956 [35] considered the phase of a beam of light as it changed state of polarization. His most important result can be explained in two parts. The first part found that the interference between two beams in non-orthogonal states can be defined as

$$(\langle A| + \langle B|)(|A\rangle + |B\rangle) = 2 + 2|\langle A|B\rangle|cos(ph\langle A|B\rangle) \tag{3.6}$$

where $|A\rangle$ and $|B\rangle$ are two non-orthogonal beams in different states of polarization [35]. When the two beams are in phase, the term $ph\langle A|B\rangle$ is considered to be real and positive [35].

The second contribution made was showing that the connection has the property of non-transitivity [35]. That is to say if a beam of light in $|A\rangle$ is in phase with another beam of light $|B\rangle$ and another beam $|C\rangle$ is in phase with $|B\rangle$ then $|A\rangle$ does not necessarily have to be in phase with $|C\rangle$ [35]. From this two part connection, it was proposed by Pancharatnam that if $|C\rangle$ was in the same state of polarization as another state $|A'\rangle$, there will exist a phase difference when a beam changes state through the path ABC as shown in figure 3.1(b) such that

$$\langle A|A'\rangle = exp\left[-i\frac{\Omega_{ABC}}{2}\right] \tag{3.7}$$

where Ω_{ABC} is the solid angle formed by the triangle ABC on the Poincaré Sphere as shown in figure 3.1(b) [35].

This can be related to Berry's Phase from Quantum Mechanics if we consider a spin-1/2 particle in a two state quantum system that is parallel transported along a closed path formed by the same geo disc shown in figure 3.1(b) [3]. This process is considered to be Adiabatic as its state changes slowly as it travels along the closed path which gives us the condition for Berry's Phase

$$< \psi|U|\psi > /dt = 0 \tag{3.8}$$

where U is the operator acting on the system due to the parallel transport of the polarization state along the Poincaré sphere and is given by

$$U = Texp\left[-i\int_0^T dt'\omega(t') * \sigma\right] \tag{3.9}$$

where T is the time it takes to travel around the closed path, σ is the quantum number for an electron ($\sigma = \pm 1/2$) and $\omega(t')$ is the instantaneous angular velocity of the tangential vector being parallel transported along the closed path [3]. If the integral is just the angle forming a closed path on the sphere between states $|A\rangle$ to $|B\rangle$, the phase difference between $|A'\rangle$ and $|A\rangle$ is given by

$$< A|A' >= exp\left[-i\frac{\Omega(C)}{2}\right] \tag{3.10}$$

where C is the closed path formed by points ABC on the Poincaré sphere. This implies that the Pancharatnam connection is an Adiabatic process described by Berry's phase as both methods generate the same result [3]. It is important to note that because the formulae derived for the phase difference only depend on the connection in 3.8, the change in polarization does not need to be slowly varying as predicted in Adiabatic theory [3]. This is convenient as polarization changes in experiments are sudden as they occur from projections onto a certain axis of polarization. The phase shift can be detected by measuring interference.

This result confirms with an effect later proposed by Aharanov and Bohm stating that the phase shift accumulated by two beams of electrons is directly proportional to the magnetic flux they enclose [3]. When speaking of polarized light, the magnetic flux is the solid angle of the closed path on the Poincaré sphere.

Pancharatnam's predicted phase is not due to birefringent materials or of dynamic origin. It is purely determined by the change in polarization states forming a closed path on the Poincaré sphere [3]. This theory can be used in the design of

new thin film optical elements to manipulate beams of light.

3.2 K-Space

Another way of describing Geometric phase of a photon is in momentum space from a quantum mechanical perspective [42]. A geometric phase can be acquired by a photon as it propagates along a single mode fiber wound in the shape of a helix. The phase acquired does not come from optical activity induced on the fiber due to the elasto-optic effect or torsional stress when the fiber is twisted into a helix [42]. The phase difference acquired is only dependent on the geometry of the helix and hence the path traveled by the photon [42]. As long as the path subtended by the photon is closed in momentum space, the angle of rotation of the polarization of light in Cartesian space does not depend on the path of the fiber [42]. This only applies for optical fibers that have a path that varies in three dimensions. Planar paths show no significant rotation of the direction of polarization as the photon propagates [42]. This is another aspect that shows the phase change is geometric and not dynamic. Chiao proposed and performed an experiment using a He-Ne laser and linear polarizer at the input and output of an optical fiber [42]. The fiber was inserted in a Teflon sleeve and wound into case 1: a uniform helix with a constant pitch angle and case 2: a non-uniform helix with varying pitch angle [42]. To ensure no torsional stress, the fiber was left free to move at the output [42]. For the photon to travel around a closed loop in momentum space, the fiber direction had to be oriented the same way at the input and output [42]. For case 1: The arc length of the fiber was constant but the radius and pitch angle of the fiber was varied by attaching the fiber to a spring [42]. Berry's phase for uniform one turn helix is given by

$$\gamma(C) = -2\pi\sigma(1 - \frac{p}{s}) \tag{3.11}$$

where p is the pitch length, and s is the arch length of the fiber [42]. σ is the helical quantum number, either +1 or -1. σ will be +1 here to measure the rotation of linearlly polarized light, predicted from quantum theory [42]. When this theory is plotted with the experimental results, good agreement is found by Chiao [42]. This shows that the phase acquired is purely geometric and there are no other contributing factors [42].

In case 2, for a non uniform helix, the pitch angle of the helix was varied according to the equation

$$\theta(\phi) = tan^{-1}(r\frac{d\phi}{dz}) \tag{3.12}$$

where r is the radius of the cylinder the fiber was placed in and ϕ is the coordinate of the helix corresponding to the cylindrical coordinate system (r,ϕ,z) [42]. For a non-uniform sphere, the solid angle will be

$$\Omega(C) = \int_0^{2\pi} [1 - cos(\theta(\phi))] d\phi \tag{3.13}$$

which leads to Berry's phase predicting [42]

$$\gamma(C) = -\sigma\Omega(C) \tag{3.14}$$

Plotting the above equation vs solid angle traveled by the photon in momentum space gives good agreement as shown in [42]. Error arises from small optical rotations due to torsional stress or the fact one end of the fiber was able to hang freely during measurements in the experiment [42]. This shows that the phase seen is purely Geometric and not due to any material birefringence or torsional stress placed on the fiber which was minimized during the experiment [42]. Figure 3.2 shows the path of the tangent vector of the optical fiber as it travels around a closed loop in K-space or momentum space.

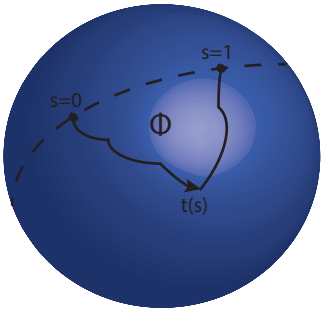

Figure 3.2: As an optical fiber is wound in a helix, the local tangent vector of any point on the helix can change and form a closed path. The total geometric phase difference from a beam at point s=0 and point s=1 will be equal to the area subtended by the closed path formed by the change in local tangent vector on the momentum sphere.

3.3 Samuel Experiment

The main requirement to see a geometric phase between two beams of light is the light must travel over a closed path. In the paper by Samuel et al [33], an interferometry experiment is proposed to show Geometric Phase. A diagram of the experiment is shown in figure 3.4(a). Unpolarized light from a He-Ne laser at a wavelength of 633nm is converted into left circularly polarized light (LCP) by a +45 linear polarizer and quarter wave plate [33]. The LCP then is split equally into two beams that

travel in opposite directions around the interferometer as shown in figure 3.4(a). In the bottom segment of the closed loop, a rotatable linear polarizer is placed with an axis of polarization oriented at an angle, θ with respect to the $\overrightarrow{y}$ axis. We will define the two beams as beam 1 and beam 2 [33]. Beam 1 travels clockwise around the loop and beam 2 travels counter clockwise [33]. The two beams are then recombined at the beam splitter and sent through a circular polarizer that converts the linearly polarized light to right circularly polarized light (RCP) [33]. A photo diode then measures the output intensity of the beam normalized to an input intensity of 1 for different angles of the rotatable linear polarizer [33]. The output intensity is an interference pattern for varying angles of the rotable linear polarizer [33]. For an interference pattern to occur, there must be a phase difference between the two recombined beams [33].

Traditionally, the biggest criticism to the existence of geometric phase and validity of experiments is the presence of optical elements that create phase differences in light by using birefringent crystals. In this experiment, there are no dynamic phase elements such as wave plates. All optical elements are purely projectional. All polarization states are achieved by projecting the previous state onto the optical axis of the optical element the light goes through so only electric field components with their direction parallel to the optical axis of the element are transmitted. The solid angle subtended on the Poincaré Sphere for each beam in this experiment is shown in figure 3.4(b). It is found that that the total solid angle is (8θ) and the total phase difference will be (4θ). The intensity pattern measured experimentally by the photo diode is exactly predicted by Pancharatnam theorem in Samuel et al [33].

3.3.1 Jones Matrix Treatment

A common way to represent the polarization state of light is through the Jones Matrix. From the Samuel experiment, both beam 1 and beam 2 can each be analyzed this way by starting with the original state of polarization of LCP light for both beams. This polarization state is represented as a 2x1 Jones Vector. The effect of each optical element the light beam encounters can be found by multiplying the Jones vector by a 2x2 Jones Matrix. Beam 1 is analyzed first. The Jones vector for LCP light is given by

$$J_{LCP} = \frac{1}{\sqrt{2}} \begin{bmatrix} 1 \\ i \end{bmatrix} \tag{3.15}$$

The first optical element the beam 1 encounters is the linear analyzer at some angle (θ). The Jones matrix for this is found by using the 2x2 rotational matrix to project the linear polarizer at angle (θ) onto the vertical $\overrightarrow{y}$ axis, multiplying by the Jones

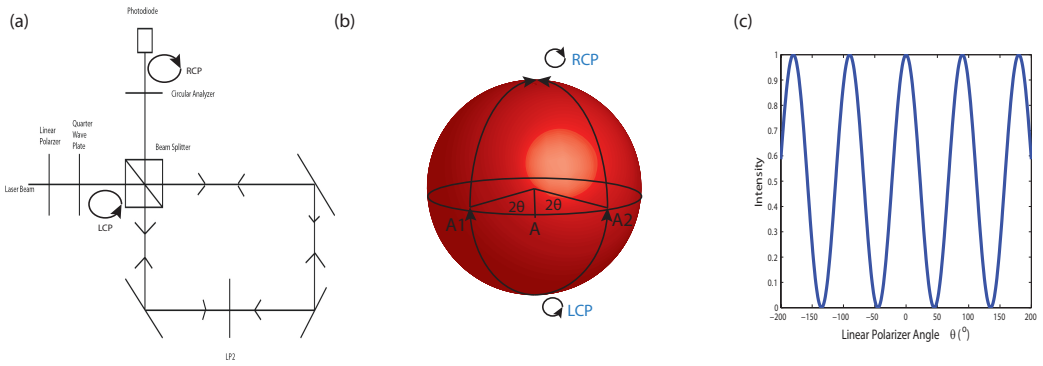

Figure 3.3: (a) Experimental Setup of an interferometry experiment where left circularly polarized light is sent through a beam splitter and two beams travel in opposite directions around a closed path and are brought back together through the same beam splitter. The output intensity is measured as a function of polarization angle to see a phase difference between the two beams resulting from optical elements using pure projections. (b) The phase change of the two light beams as shown on the Poincar Sphere. The total phase change is equal two half the solid angle subtended on the Poincaré Sphere. (c) The measured output intensity at the photo diode from the Samuel experimental setup when the linear analyzer in the interferometry loop is continuously rotated through an angle θ.

Matrix of the polarizer, and then projecting back onto the axis of the polarizer oriented at angle (θ). The total Jones matrix for the linear polarizer at angle(θ) is given by

$$J_{LP1} = \begin{bmatrix} sin^2(\theta) & -sin(\theta)cos(\theta) \\ -cos(\theta)sin(\theta) & cos^2(\theta) \end{bmatrix} \tag{3.16}$$

When multiplied by the Jones vector for LCP light, the resulting Jones vector is

$$J_1 = \frac{1}{2 * \sqrt{2}} \begin{bmatrix} -isin(\theta)e^{i\theta} \\ icos(\theta)e^{i\theta} \end{bmatrix} \tag{3.17}$$

Finally, multiplying (J_1) by the Jones matrix for a RCP polarizer, we get a final result for the polarization state for beam 1 at the detector

$$J_{1final} = \frac{-e^{i2\theta}}{2\sqrt{2}} \begin{bmatrix} 1 \\ -i \end{bmatrix} \tag{3.18}$$

For beam 2 traveling in the opposite direction, the only changes in the Jones analysis is in the linear polarizer at an angle (θ). The polarizer is rotated at an angle of $(-\theta)$ instead of θ). The Jones matrix for for the rotatable linear polarizer for beam 2 becomes

$$J_{LP2} = \begin{bmatrix} sin^2(-\theta) & -sin(-\theta)cos(-\theta) \\ -cos(-\theta)sin(-\theta) & cos^2 - (\theta) \end{bmatrix} \tag{3.19}$$

This leads us to the final result given by

$$J_{2final} = \frac{-e^{-i2\theta}}{2\sqrt{2}} \begin{bmatrix} 1 \\ -i \end{bmatrix} \tag{3.20}$$

A phase term is found outside the Jones Vector of each beam after travelling the closed path. For the beam 1, it is $(+2\theta)$ and for beam 2, (-2θ) due to beam 2 travelling in the opposite direction of beam 1. The total phase difference between beam 1 and beam 2 is given by

$$\Delta\Phi = 4\theta \tag{3.21}$$

This result agrees with Pancharatnam's theorem [33]. The resulting intensity seen for RCP light with a (4θ) phase difference calculated above is plotted in figure 3.4(c). The resulting Jones Matrix parameters plotted in figure 3.4(c) match the experimental results measured by Samuel [33]. It has been proven here that the geometric phase is seen using a simple Jones matrix treatment of an interferometry experiment using purely projectional elements over a closed loop subtended along the Poincaré sphere.

3.3.2 Stokes Parameter Treatment

Stokes Parameters are another set of values that describe the state of polarization of light. Unlike Jones matrices, they are able to handle states of partial polarization. The Stokes Vector is a 4x1 vector with the first term represented by the size of the Poincaré sphere (usually 1) and the last three terms representing the $\overrightarrow{x}$, $\overrightarrow{y}$, and $\overrightarrow{z}$ axes of the Poincaré sphere, respectively. Optical systems are represented by Mueller matrices. Mueller matrices apply a linear transformation on the Stokes vectors. A Mueller matrix can be derived numerically from the Jones matrix in the case of total polarization. In the case of the Samuel experiment, a phase shift of (4θ) can be derived through a Stokes treatment of the system as shown below. The rotational Mueller matrix can be derived from the Jones matrix and is defined as

$$R(\theta) = \begin{bmatrix} 1 & 0 & 0 & 0 \\ 0 & cos(2\theta) & sin(2\theta) & 0 \\ 0 & -sin(2\theta) & cos(2\theta) & 0 \\ 0 & 0 & 0 & 1 \end{bmatrix}$$

The Stokes vector for a linear polarizer

$$S_{LP} = \begin{bmatrix} 1 & -1 & 0 & 0 \\ -1 & 1 & 0 & 0 \\ 0 & 0 & 0 & 0 \\ 0 & 0 & 0 & 0 \end{bmatrix}$$

The Stokes vector for a right circular polarizer RCP is

$$S_{RCP} = \begin{bmatrix} 1 & 0 & 0 & 1 \\ 0 & 0 & 0 & 0 \\ 0 & 0 & 0 & 0 \\ 1 & 0 & 0 & 1 \end{bmatrix}$$

The stokes vector of the incident left circularly polarized beam 1

$$S_{LCP} = \begin{bmatrix} 1 \\ 0 \\ 0 \\ -1 \end{bmatrix}$$

Consequently the resultant path of the beam traveling in the positive direction can be calculated in a similar way as the Jones Vector.

$$S_{1final} = \frac{1}{4} * RCP * R(-\theta) * LP * R(\theta) * I$$

The Stokes vector for beam 1 prior to going through the right circular polarizer has the Stokes vector

$$S_{1final} = \begin{bmatrix} 1 \\ cos(-2\theta) \\ sin(-2\theta) \\ 0 \end{bmatrix}$$

The same procedure is identical for the beam passing in the opposite direction except that the linear polarizer is rotated by $(-\theta)$. In this manner we obtain a Stokes vector of

$$S_{2final} = \begin{bmatrix} 1 \\ cos(2\theta) \\ sin(2\theta) \\ 0 \end{bmatrix}$$

After multiplication with the RCP the same result is obtained for both vectors

$$S_{final} = \begin{bmatrix} \frac{1}{4} \\ 0 \\ \frac{1}{4} \\ 0 \end{bmatrix}$$

From this we can see that the beams do not differ in degree of polarization however, there is a phase difference obtained from a phase of (-2θ) from the beam traveling in the positive direction, and a phase change of (2θ), from the beam traveling in the negative direction, creating a total phase change of (4θ).

3.4 Geometric Phase Optical Elements

Linear polarizers are readily available to use in experiments in the form of sheets or prisms [18]. Circular polarizers are not as common and more difficult to create. Circular polarizers work by reflecting/absorbing one type of circular polarization and transmitting the other. In Samuel et al [33], a liquid crystal film is proposed as a material for a circular polarizer. However, a different approach is proposed here using a film of helical gold nanowires as shown below in figure 3.5(a). Gold is chosen as the choice of material as it is a very good conductor in the mid infrared region and does not suffer from the high loss it does in the visible and near infrared region. With the development of GLAD by Brett et al [26], gold helical nanowires are a structure that can be fabricated by a rather straight forward process. A plot of the simulated transmission for right circularly and left circularly polarized light incident on the film is shown in figure 3.5(b). RCP is strongly transmitted over the entire region of 3-10 μm while LCP is reflected/absorbed for the region between 3μm and 5μm. The resonance is not plasmonic as it is too far away from the plasma frequency for gold but is rather due to the standing wave condition being met for a helical structure with 2 full turns as seen in figure 3.5(a) along with the handedness of the helix [18]. When the Bragg condition is met for the combination for all the helical wires, the complete transmission of RCP happens at a wavelength of approximately 4.8μm. A wider bandwidth of operation is seen when compared to the analyzer used by Samuel [33]. The helical nanowires have been designed to have a wire thickness of 5nm, helix radius of 5nm and length of 2μm. The helix radius and pitch of the helix can be adjusted to change the wavelength region to which the analyzer can operate in.

This is one example a design of a metamaterial which can help understand geometric phase. Other designs have been proposed in [10, 18, 46]. With the advancement of fabrication procedures and introduction of GLAD [26] to fabricate helical nanowires, it should be possible to measure Geometric Phase with ultra thin

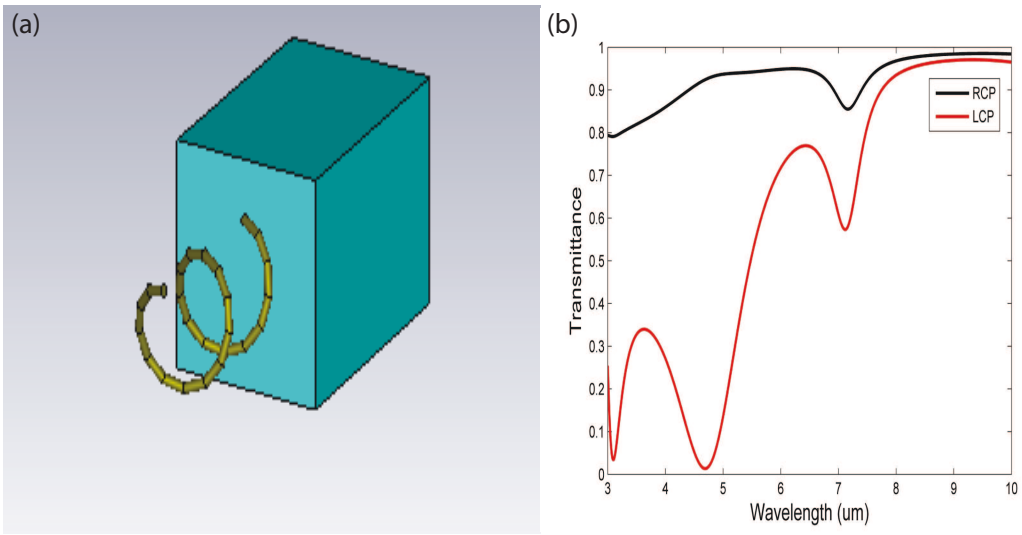

Figure 3.4: (a) Structure of a unit cell of gold helix with wire radius 5nm, helix radius 50nm, and length of $1\mu m$ for a circular polarizer. (b) The transmission of LCP and RCP is shown for the helical nanowire structure. LCP is transmitted and RCP is completely reflected or absorbed at a wavelength of $4\mu m$. This wavelength can be tuned by changing the wire radius, and helix radius to act as a circular polarizer at any wavelength. This optical element can help design optical experiments that are related to the geometric phase of light.

projective optical elements.

Chapter 4

All Dielectric Anisotropic Metamaterials

The discovery and development of nanophotonics and new nanofabrication techniques for light guiding in the last decade have led to strong efforts to miniaturize and integrate electrical and photonic components for many on-chip applications [24, 22, 23]. The integration of photonic components into electronic circuitry has also increased the speed of modern communication and computation systems. Two main problems exist in conventional photonic components. One is the propagation of information below the diffraction limit and the other is cross talk between components on densely packed silicon photonic circuits [24, 22, 23]. One approach proposed to beat the diffraction limit was the plasmonic waveguide. This design tries to take advantage of the surface plasmon modes that exist and that can be excited in metals [24, 22, 23]. Surface plasmons can carry sub diffraction limit information as propagating waves. However, with the introduction of metals into the waveguide, additional losses (absorption) occur and light can not propagate more than a few microns [24, 22, 23]. Another issue with the plasmonic waveguide is the absorbed light is dissipated as heat which can overheat and destory electronic components on the silicon chip. A better approach is needed without the use of metals to confine more power inside waveguides.

A new class of waveguides have recently been introduced [24, 22, 23] called extreme skin depth waveguides. Sub diffraction information can be confined inside the core of a 1D dielectric waveguide. If the slab size of the waveguide is small enough, both TE and TM modes can propagate without any cutoff [24, 22, 23]. In a conventional waveguide, these modes leak extensively into the cladding [24, 22, 23]. With an anisotropic all dielectric metamaterial as a cladding, the skin depth of evanescent waves leaking into the cladding can be decreased, confining more power inside the core [24, 22, 23].

Total internal reflection (TIR) is the main mechanism for guiding light. It was first discovered in 1611 by Johannes Kepler but it was not until almost 200 years later before it was proposed it could be used for guiding or confining light [24, 22, 23]. Guiding and confining light is important in many applications, including, nanowaveguiding, laser cavities, and TIR fluorescence microscopes [24, 22, 23]. The law of total internal reflection states that if the index of refraction for light in an incident medium is greater than the transmitted medium ($n_1 > n_2$), there is a critical angle of incidence for which 100% of the power carried in a propagating wave will be reflected back into the incident medium. The critical angle is defined as

$$\theta_c = \arcsin\left(\frac{n_2}{n_1}\right) \tag{4.1}$$

where θ_c is the critical angle for total internal reflection and n_1 and n_2 are the refractive indexes in the incident and transmitted medium, respectively. Any evanescent waves will decay away exponentially in the transmitted medium. This can be explained easily by examining the momentum or wave vector of the wave at the interface between the incident and transmitted medium (section 4.1).

A conventional design for confining light works by guiding light inside a core material that acts as the incident medium by multiple reflections, all of which satisfy the TIR condition. The core has a higher refractive index than the transmitted medium which is called the cladding material, designed to be of lower index for the TIR condition to be valid. The confinement is based entirely on the refractive index contrast between the core and the cladding. To date, the best design achieved for a waveguide has been with a core made of silicon (n = 3.5 @ 1.55 μm) surrounded by vacuum (n =1) as the cladding material. If the core size is sub wavelength, less than 2% of the total power is confined inside the core [24, 22, 23]. Another possible waveguide design confines light via Bragg reflection in the band gap of photonic crystals [24, 22, 23]. The main problem with both of these designs, is it focuses on the confinement of only propagating waves. The issue of power loss to evanescent waves decaying into the transmitted medium still exists.

With the emergence of metamaterials in the last decade, the laws of refraction and reflection have been revisited in order to study their properties when the incident or transmitted medium is a metamaterial with high anisotropy. With high anisotropy, we can control both the confinement of propagating and evanescent waves inside the core of the waveguide with a phenomenon first proposed by Jahani et al [24, 22, 23] known as relaxed total internal reflection.

4.1 Relaxed Total Internal Reflection

To derive the condition for relaxed TIR, imagine a situation as described in figure 4.1(a) [24, 22, 23]. Light is incident from an incident medium (medium 1) and reflected at the interface between medium 1 and an all dielectric anisotropic transmitted medium (medium 2). The interface is defined along the $\overrightarrow{z}$ axis and perpendicular to the interface is the $\overrightarrow{x}$ axis. It has been shown recently by Jahani et al [24, 22, 23]that a sufficient condition to have total internal reflection is

$$n_1 > \sqrt{\epsilon_x} \tag{4.2}$$

for (p) polarized light [24, 22, 23] and

$$n_1 > \sqrt{\epsilon_y} \tag{4.3}$$

for (s) polarized light [24, 22, 23] where n_1 is the refractive index of medium 1 and ϵ_x and ϵ_y are the permittivity of the anisotropic dielectric medium perpendicular to the interface and parallel to the interface, respectively. It is important to note that for uniaxial multilayer metamaterials, $\epsilon_y = \epsilon_z$. Relaxed TIR has been proven by examining the conservation of momentum at the interface between the two mediums [24, 22, 23]. For (p) polarized light, the conservation of momentum condition is

$$\frac{k_{z\parallel}^2}{\epsilon_x} + \frac{k_{x\perp}^2}{\epsilon_z} = k_o^2 \tag{4.4}$$

where k_o is the wave vector in the incident medium and $k_{x\perp}$ and $k_{z\parallel}$ are the wave vectors parallel and perpendicular to the interface, respectively [24, 22, 23]. The perpendicular component of the wave vector can clearly be zero or imaginary such that it is evanescent and decays away in medium 2. The opposite case for the parallel component being zero or imaginary is true for (s) polarized light. Therefore, the critical angle for relaxed TIR is different for (p) and (s) polarized light which has never been previously shown before.

With only needing one part of the permittivity of the anisotropic metamaterial to meet the condition for TIR, we have an open degree of freedom for the permittivity in the opposing direction. This can be used to confine evanescent waves if $\epsilon_z >> 1$ for the (p) polarized light case as shown in figure 4.1(b). It has been proven that with this condition along with the condition for relaxed TIR being met using a silicon/silica multilayer anisotropic metamaterial, 36% of the total power can be confined in the silicon core compared to just 2% for a silicon core/vacuum cladding waveguide structure [24, 22, 23]. The refractive index of the core was 3.5 and the cladding is 1 for a core size of 150nm at an operating wavelength of 1550nm [24, 22, 23]. The anisotropic metamaterial cladding had permitivitties of $\epsilon_z = 15$

and $\epsilon_x = 1.2$ [24, 22, 23]. Proving these conditions experimentally is best done by fabricating dielectric multilayer metamaterials directly onto a prism made of silicon which will act as the core material.

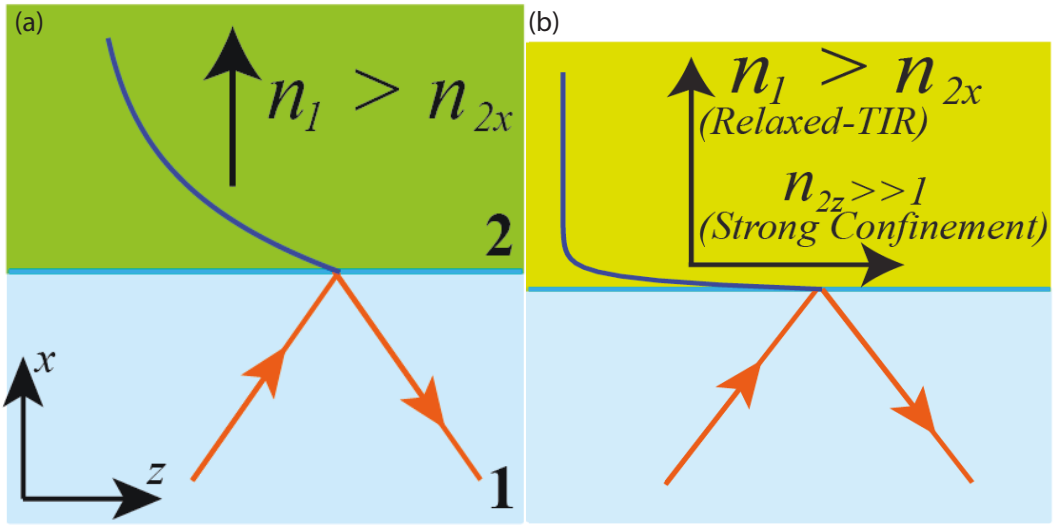

Figure 4.1: [24, 22, 23] (a) Relaxed Total Internal Reflection requires that the refractive index of medium 1 is greater than medium 2 in the x direction and the incident angle is greater than the critical angle for TIR. If the TIR condition is met, light will be totally reflected back into medium 1 with only evanescent waves decaying into medium 2. (b) If the refractive index in medium 2 in the z direction is made very large, higher confinement of power in medium 1 results.

4.2 Fabrication of Si/SiO2 Multilayer Anisotropic Metamaterials

To create our all dielectric metamaterial, we will use the simple multilayer design. Silicon and silica were used as the alternating layers for our multilayer stack as they have low loss at our operating wavelength of 1.55 μm (telecommunication wavelength) and can easily be fabricated and integrated as the cladding material onto silicon waveguide photonic circuits. However, using the silicon and silica design, we emphasize that it is difficult to acheive the ideal situation where the refractive index is as low as possible perpendicular to the core/cladding interface and as high as possible parallel to the interface. Silicon and silica were fabricated using magnetron sputtering and magnetron reactive sputtering. BK7 microscope slides, BK7 right angle prisms, and hemicylindrical silicon prisms were used as substrates for our samples. The reasoning for depositing on the prisms is it would be easier to perform total internal reflection measurements when depositing directly onto prism

as there was no index matching fluid readily available at a refractive index of n=3.5 for the silicon prism. A special apparatus was built to hold the prisms during deposition inside the vacuum chamber and that could be easily be attached to the existing substrate holder. A photo of the apparatus is shown in figure 4.3(a). With the new substrate holder and the thickness of the prisms, the film properties would change and the sputtering conditions had to be altered as the surface the silicon and silica thin films were to be deposited on was much closer to the target than with the original substrate holder. With moving the substrate closer to the target, this produced lossier films with a higher refractive index. With loss being a key contributing factor to power loss in waveguides, the loss had to be reduced. Reducing the deposition power produced low loss films on the new substrate holder as confirmed by ellipsometry measurements and fitting for the refractive index and extinction coefficient.

Silicon and silica were both deposited at a power of 150W using a pulsed power supply at a frequency of 150kHz and off time of 0.5μs for silicon and 0.8μs for silica. The targets were ramped up to deposition power very slowly in order to prevent thermal shock and ensure they would last for many depositions as silicon is a fragile material to sputter.

A total of 5 periods of silicon/silica were fabricated at fill fractions of 0% (pure silica), 30%, 50%, 70%, and 100% (pure silicon) on BK7 prisms. The 100% pure silicon sample was not fabricated on the hemicylindrical silicon prisms. The total thickness of each period was kept constant at 100nm and only the ratios of silicon to silica within each period were altered to change the fill fraction. This gave the total thickness of the structure to be 500nm for all fill fractions. For the 0% filling fraction, 500nm film of silica was deposited and for a 100% filling fraction, 500nm of silicon was deposited. These were used as control samples to prove the principle of relaxed total internal reflection.

A 200nm thick layer of tungsten was deposited on top of the multilayer structure at each fill fraction to prevent any additional evanescent waves from tunneling outside the silicon prism that passed through the multilayer structure. Tungsten was deposited at a power of 300W via magnetron sputtering using a pulsed power supply with 150kHz and 0.5 μs off time.

4.3 Characterization of Si/SiO2 Multilayer Anisotropic Metamaterials

Initial characterizations of our structure were performed using ellipsometry on the samples deposited on BK7 microscope slides. ψ is the basic parameter used in ellipsometry and can be defined as

$$\frac{r_p}{r_s} = tan(\psi)e^{i\delta} \tag{4.5}$$

where rp and rs are the complex reflection coefficients from the sample. ψ is the magnitude of the ratio between rp and rs and δ represents the phase difference between (p) polarized and (s) polarized reflectance. For all samples, there is a minimum point in the value of ψ over the wavelength range from 1 to 1.7μm. For a fill fraction of 30%, figure 4.2(a) shows the minimum in ψ at an angle of 30^o. Figure 4.2(b) shows the location of the minimum in ψ vs changing fill fraction. Simulations were performed using both EMT and Transfer Matrix Method (TMM). Good agreement is shown between both simulation methods as well as experimental methods indicating that the values for the thickness and refractive index for silicon and silica used in future simulations are very close to what we measure experimentally. Initial fitting of the refractive index, extinction coefficient, and thicknesses were accurately fitted for a single film of silicon, silica, and tungsten in order to have accurate parameters for each layer for future simulations. We chose the method of comparing the minimum point of ψ to characterize our structure as anisotropic modeling of many layered structures is complicated and produces a very large error in the fitting algorithm.

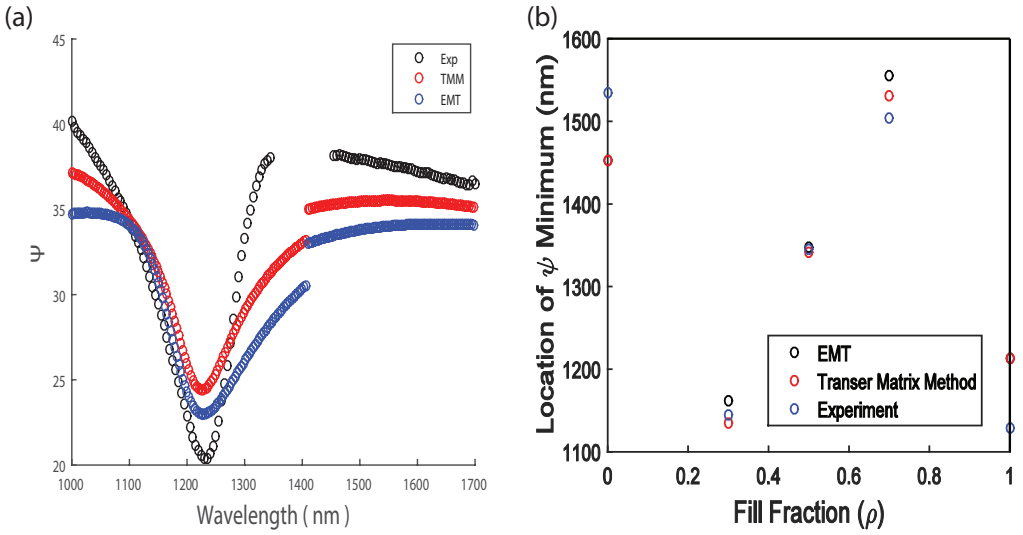

Figure 4.2: (a) ψ vs wavelength at an incident angle of 30^o for a sample of filling fraction of 30% for experimental measurements, TMM, and EMT. (b)The minimum in ψ is plotted with change in fill fraction and compared for EMT, TMM, and experimental measurements. Both analytical methods agree with experimental results for trend and magnitude of ψ.

4.4 Total Internal Reflection Measurements of Si/SiO2 Multilayers on BK7 Prisms

BK7 right angle prisms were the first prisms that multilayer structures were deposited on as they were relatively cheap and there was no lensing effect on the laser beam as there was with hemicylindrical silicon prisms. The prism with the multilayer structure was placed on a rotation stage and was illuminated with a TR labs prototype 1530nm narrow line width laser. The laser output was coupled into a collimated single mode fiber. The beam then went through a linear polarizer that was rotated to switch between (p) and (s) polarization, depending if we were measuring R_p or R_s, before it was incident on the prism. The output spectrum vs angle was then measured after the beam went through the prism, was reflected off the longest side of the prism with the multilayer structure on it and then back out of the prism as shown in figure 4.3(b). The incident angle was increased in increments of 2^o from 10^o to 80^o. A Newport Optics Optical Power Meter calibrated to a wavelength of 1530nm was then used to measure the reflected power. The incident power before going into the prism was measured and then the reflectance was plotted by dividing the reflected power by the incident power for each angle measured for both (p) and (s) polarized light.

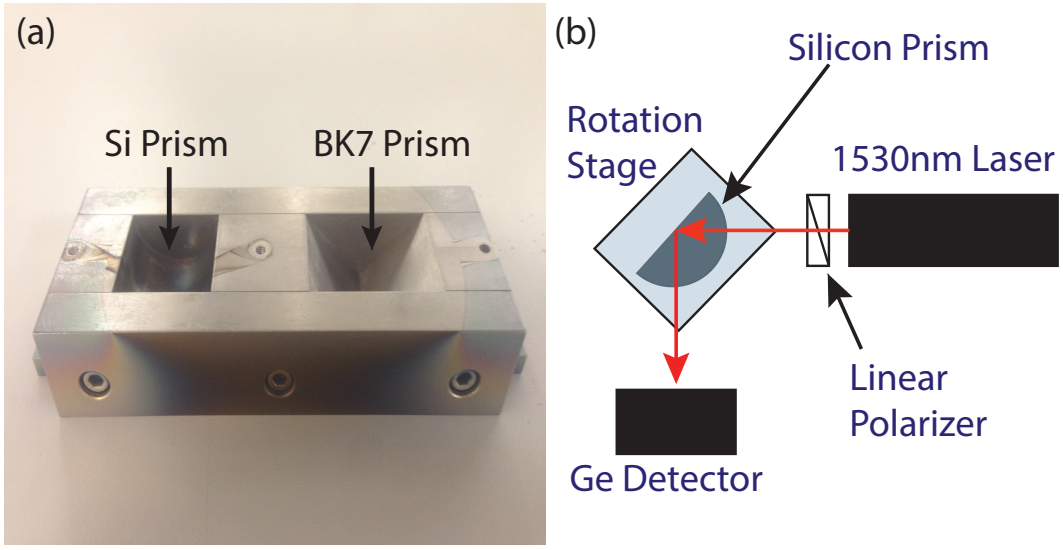

Figure 4.3: (a) The deposition appartus used to mount BK7 glass and silicon prisms for sputtering of multilayer metamaterials. (b) Experimental Setup for Total Internal Reflection measurements.

In a waveguide light, is guided along the core and is not transmitted from one medium into another. In our TIR prism setup, light is transmitted from the air/prism interface into the prism and from the prism back into air at the prism/air

interface. These two reflections in the optical path need to be accounted for. The total transmitted power through the prism can be derived by multiplying the fresnel transmission coefficeients together from each interface to give

$$T = \frac{(4n_1n_2)^2}{(n_1 + n_2)^4} \tag{4.6}$$

where n_1 is the index of air and n_2 is the index of BK7 glass(n=1.48). This leads us to find the reflectance in a waveguide situation via the relation

$$R = \frac{R_{measured}}{TI_{measured}} \tag{4.7}$$

where R is the reflectance in a waveguide, $I_{measured}$ is the incident measured power, and $R_{measured}$ is the measured reflected power. The results for fill fractions of 0%, 30%, 50%, 70%, and 100% are shown in figures 4.4(a)-(e). The experimental results are plotted against TMM simulations for our multilayer structure. There is a discrepancy for (s) polarized reflection in the 30% sample and for (p) polarized light in the 100% fill fraction sample. This can be attributed to our silicon thin film being slightly less lossy then the films simulated.

Most results showed agreement with minimum discrepancies which meant that our experimental method and multilayer structures were working as expected. The next step was to deposit on hemicylindrical silicon prisms where silicon would act as the core material to show two different critical angles for (p) and (s) polarized light to prove relaxed TIR.

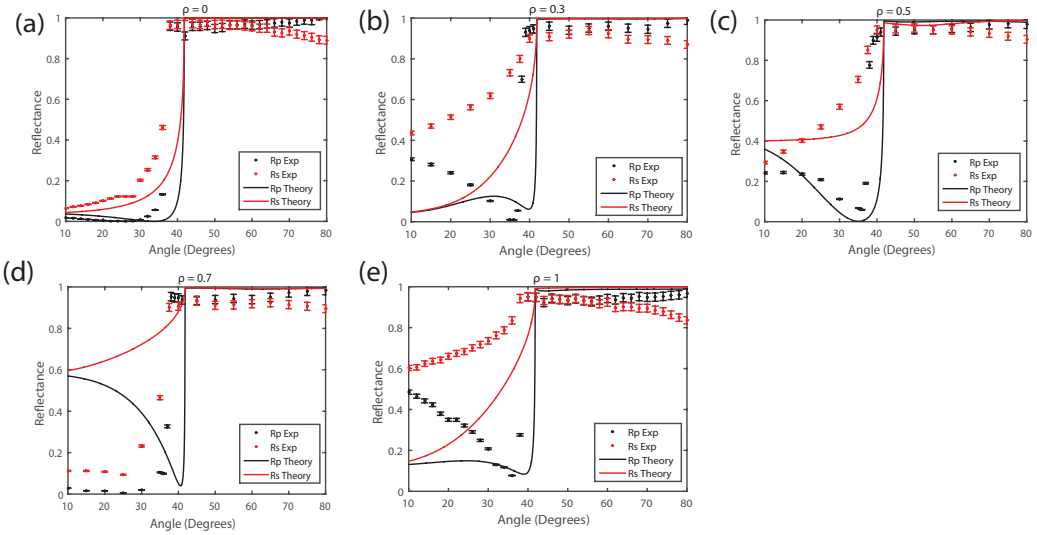

Figure 4.4: (a)-(e) show TIR measurements (experiment and theory) for 5 periods of Si/SiO2 deposited directly on a BK7 glass right angle prism for fill fractions of p=0%, 30%, 50%, 70%, and 100% respectively.

4.5 Si/SiO2 Multilayer Anisotropic Metamaterials on Hemicylindrical Silicon Prisms

5 period (100nm periodicity) silica/silicon multilayer structures were deposited to give a total metamaterial thickness of 500m on the hemicylindrical prisms with the 200nm absorbing tungsten layer on top to absorb any additional evanescent waves that propagated through the multilayer structure. The resulting reflection spectrum was measured and plotted vs angle with the same method as described in equations 4.6 and 4.7 before, except n_2 was changed to be the refractive index of silicon (n=3.5) when accounting for the two reflections. The TIR prism set up is shown in figure 4.5(a) with the multilayer structure and absorber being deposited on the long flat face of the prism. Samples with filling fraction of 0%, 30%, 50%, and 70% were fabricated, each having the absorbing tungsten layer. A 100% filling fraction sample was not fabricated as depositing silicon onto silicon would just lead to a critical angle of 90^o for both (p) and (s) polarized light.

Figure 4.5(b) shows the reflection spectrum for a 30% filling fraction sample. As we can see (p) polarized light has a critical angle for total internal reflection of 36^o and (s) polarized light of 46^o as predicted by using an anisotropic all dielectric cladding material. Above the critical angle, the reflectance is showed to slightly increase as we approach higher angles and not stay constant at 100% reflection as predicted by simulations. This can be attributed to higher loss in the structure and the absorbing layer than used in simulations. Error bars show a small discrepancy for the measurable errors in this experiment. Uncertainty in the detector and power meter were used to calculate the uncertainty. Additional uncertainty comes from alignment of the prism with the prism surface normal vector at each angle. The beam size is 0.5mm and hence the edges of the beam do not transmit at exactly the surface normal of the prism and will have different a different reflectance than the center of the beam.

In figure 4.5(c), the locations of the critical angle for (p) and (s) polarized light are shown for different fill fractions fabricated. The critical angle is similar for 0% filling fraction sample for (p) and (s) polarized as predicted by simulation as this structure shows no anisotropy. Error for the 0% filling fraction comes from the finite thickness of our multilayer structure. (p) and (s) polarized light will only have the same critical angle for the situation in figure 4.1(a) where each medium is infinite in thickness. This discrepancy does not occur for other fill fractions, hence the smaller error bars at higher fill fractions. The location of the critical angle for (p) and (s) polarized light changes with fill fraction as predicted by the TMM simulations as the refractive index of the multilayer structure will change for both the $\overrightarrow{z}$ and $\overrightarrow{x}$ directions with change in the effective medium parameters. This experimental work

is the first evidence of relaxed total internal reflection.

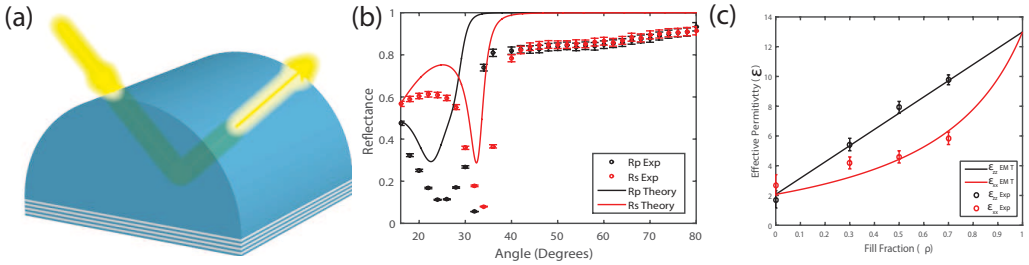

Figure 4.5: (a) Experimental Setup for measuring total internal reflection of Si/SiO2 multilayers on a silicon hemicylindrical prism. (b) Reflectance Experiment vs Theory for (p) and (s) polarized light measured for 5 periods of 30nm silicon, 70nm silica ($\rho = 30\%$). (c) Fill fraction vs critical angle for (p) and (s) polarization for 5 periods of varying fill fractions on hemicylindrical silicon prism for experiment and theory.

Chapter 5

Thermal Applications and Future Work

One of the biggest issues with using plasmonic resonances in nanostructures for metamaterials is the unavoidable loss associated with the metallic component. In the infrared and visible region, this loss is quite high and applications requiring high reflection or transmission are not practical. With high loss comes high absorption which naturally would lead one to focus on applications that benefit instead of suffer from high absorption. Thermal camouflage or cooling prevents a hot object from being detected by infrared detectors [11]. This can be observed when thermal radiation from a hot object is absorbed by another material and redirected into the regions of the spectrum other than infrared [11]. This is useful for military applications where thermal camouflage is often required [11].

The design of a device for thermal camouflage needs to act as a broadband mirror for the solar part of the atmospheric absorption spectrum and behave as a great absorber in the atmospheric transparency window for wavelengths of 8-13 μm [11]. We will start our design of the structure by focusing only on the atomspheric transparency window and defining the net cooling power of a photonic structure at temperature T, when placed in sunlight to be

$$P_{net}(T) = P_{radstruc}(T) - P_{atm}(T) - P_{absstruc} \tag{5.1}$$

where $P_{radstruc}(T)$ is the power radiated into the atmosphere by our photonic structure, $P_{atm}(T)$ is the absorbed power due to atmospheric radiation, and $P_{absstruc}(T)$ is the power absorbed by the structure [11]. The power absorbed by the structure is defined as

$$P_{absstruc}(T) = A \int_0^\infty d\lambda \epsilon(\lambda, 0) I_{AM}(\lambda) \tag{5.2}$$

[11] and the power radiated by the structure is

$$P_{radstruc}(T) = A \int d\Omega cos\theta \int_0^\infty d\lambda I_{BB}(T,\lambda)\epsilon(\lambda,\theta) \tag{5.3}$$

Kirchhoff's law states that the radiative emission and absorption of electromagnetic radiation remain in equilibrium. We therefore may consider the absorption spectrum to equal the emission spectrum for the design of our structure. Most bulk materials do not have an absorption efficiency of greater than 85% in this range, so we must design a metamaterial that will have an absorption efficiency of greater than 90%. Since the bandwidth of the transparency window is so wide, it will be convenient to design our nanostructure with two different materials, each having a unique properties. Since the area of the spectrum is in the mid infrared region, phonon polariton resonances will be the mechanism for absorbance. The design here will use two different materials with overlapping phonon polariton resonances. The materials chosen are silicon carbide (SiC) with a sharp phonon resonance at 12.5 μm and quartz with a resonance at 9.3 μm. The overlapping resonances will allow for absorption across the entire transparency window from 8-13 μm. Both SiC and quartz are also very weak absorbers in the visible and near infrared region of the electromagnetic spectrum. Simulations were done using CST Microwave Studios for three different structures.

To show the possibility of camouflage, we study the absorption spectrum of three different designs. The design is adaped from publication [11] and modified for our application. The first design considered is a planar 1μm by 1μm unit cell of a SiC layer of 8 μm followed by a 2.5 μm thick layer of quartz. The inset in figure 5.1(a) shows an exact schematic of the structure. The resulting absorption spectrum is shown for (p) polarized light in figure 5.1(a) and (s) polarized light in figure 5.1(b). The structure is only absorbing from 8 to 10μm and 12.5μm to 13μm. This does not include the entire region of the spectrum in our design requirement. The absorption efficiency reaches 90% at some wavelengths in the atmospheric transparency window. However it also decreases to approximately 30% at other wavelengths in the transparency windeo because of thin film interference. A flatter absorption band with absorption efficiency of 90% or greater needs to be seen across the whole absorption window. We must consider other designs.

The second structure considered had a 1μm by 1μm unit cell with a two dimensional air gap of 0.7μm by 0.7μm centered in the middle of the unit cell. This is introduced so that the unit cells form a two dimensional array of photonic crystal structures. The schematic in the inset in figure 5.1(c) shows the exact design. The resulting absorbance spectrum is shown for (p) polarized light in figure 5.1(c) and (s) polarized light in 5.1(d). The absorbance in the 8-11μm band is higher which

is an improvement over the first design. However, this design still doesn't meet the goal because it doesn't absorb over the entire 8-13μm band requirement with greater than 90% efficiency. Another note about the design is the absoprtion efficency of the structure does not exceed that of bulk materials. Earlier it was stated that highly absorbing bulk materials for thermal applications have an absorption efficiency of 85%. The results shown shown have maximum efficiency of 85% but not for all wavelengths in the region from 8 to 13 μm.

The third design considered has the quartz layer shaped into a pyramid as shown in figure 5.1(e) inset. The purpose of this was to increase the surface area for absorption as area is a key in the equations for power absorbed and radiated as shown in equations 5.2 and 5.3. The resulting absorption spectra are shown in figures 5.1(e) and 5.1(f) for (p) and (s) polarization respectively. The results in fact show a lower absorption efficiency than the previous two designs as the maximum efficiency seen is approximately 80% and only occurs for a small range of wavelengths. The overall absorption spectrum goes from 8 to 10.5 μm which is narrower than our goal of 8-13μm.

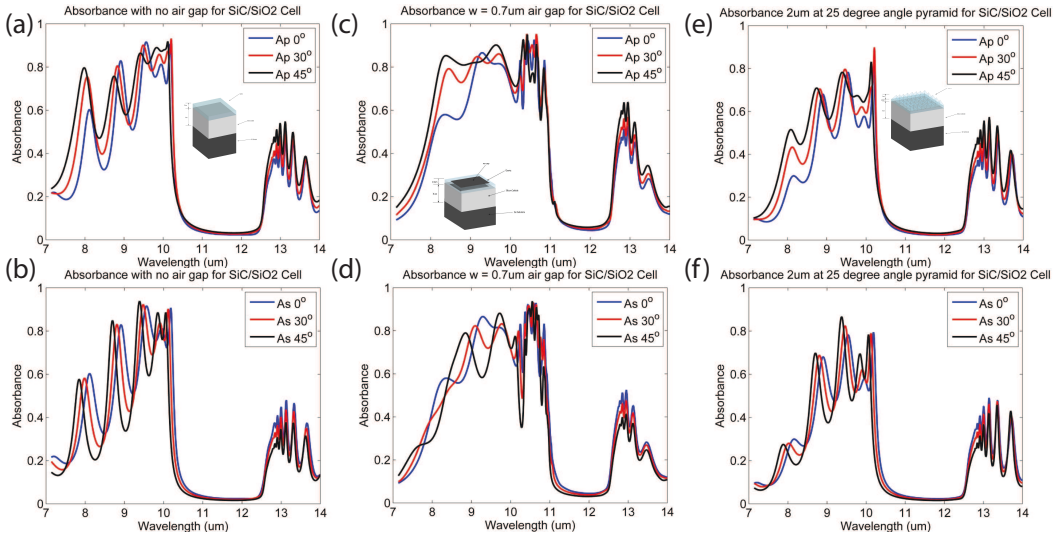

Figure 5.1: A 1μm by 1μm unit cell with 8μm of silicon carbide layer followed by a 2.5μm thick quartz layer on a glass substrate. (a) and (b) shows absorbance for (p) and (s) polarized light respectively at three different angles. (c) and (d) show absorption of (p) and (s) polarized light for the same structure as in (a) and (b) but with a 0.7μm air gap inside the unit cell so the cell behaves as a photonic crystal. (e) and (f) show absorption of (p) and (s) polarized light for a 1μm by 1μm unit cell of 8μm silicon carbide followed by a 2.5μm quartz layer shaped in the form of a pyramid to increase surface area.

An overall comparison of the three designs is shown in figure 5.2. The best design of the three was the photonic crystal structure with the air gap. It has the widest

absorption band from 8 to 11μm but does still not meet the requirements for the application. The absorption efficiency also needs to be improved so that it is higher than 90% over the entire atmospheric transparency window. However, we note that initial results show the absorption spectrum is independent of angle of incidence and polarization of incident radiation. This is a key requirement for daytime cooling of objects placed in sunlight where light is coming from all angle and is in general unpolarized.

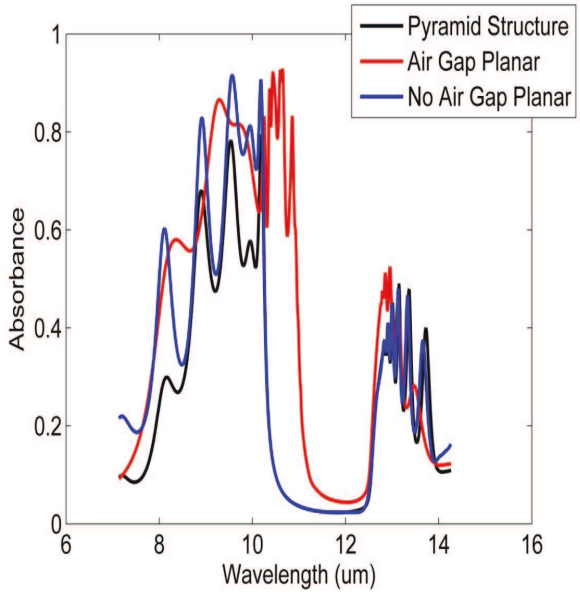

Figure 5.2: The absorption spectrum for three different designs of a thermal cooling unit cell using a pyramid structure, a planar structure, and a photonic crystal structure with an air gap. The air gap design [11] shows the widest absorption spectrum and hence is the best design.

More work must be completed in the design and simulation stage to increase the absorption bandwidth and the overall absorption efficiency. The next step will be to consider different materials with different phonon resonances. Furthermore, different structures can be studied to reach the design goals in the 8-13μm range of the electromagnetic spectrum.

Chapter 6

Summary

With the advancements of nanofabrication techniques over the last decade, it has become possible to fabricate increasingly complex nanostructure designs. This has led to metamaterials having unique electromagnetic responses for applications in quantum [19, 29, 45], thermal [39], wave guiding [13], biosensing [20, 43], and polarization manipulation [32]. We have characterized structures composed of vertically aligned gold nanowire structures exhibiting highly tunable absorption characteristics in the visible range of the electromagnetic spectrum for use in biosensing and polarization manipulation. Tilted and helical nanowires were fabricated via Glancing Angle Deposition technique as demonstrated by [26] where we characterized their optical properties using ellipsometry and spectrophotometry. These structures have a very high degree of anisotropy and can be used to manipulate the polarization of light upon reflection from or transmission through the nanostructure. This was demonstrated through simulations we performed for inclined in-plane gold nanowires. The location of the ENZ determines where the polarization manipulation occurs and can be tuned by changing the fill fraction.

When light travels along a closed path as shown in an interferometry or helically wound fiber, it can acquire a non dynamic Geometric Phase which can alter the polarization state of light. We have examined the Jones Matrices and Stokes Parameters of a closed path optical experiment such as the interferometry experiment shown in Samuel et al [33]. The Jones Matrix and Stokes Parameter treatment of light is a simple way to conclude if a geometric phase is acquired in a closed path optical experiment. A gold helical nanowire structure has been designed for use as a circular polarizer by absorbing left circularly polarized light and transmitting right circularly polarized light. The helix pitch, helix radius, and wire radius can be changed to tune the location in the mid infrared region for any application of choice. This circular polarizer can help design experiments where Geometric Phase is important.

We have shown relaxed total internal reflection has been experimentally demon-

strated using all dielectric anisotropic metamaterials as the cladding material in a silicon waveguide structure. Samples were fabricated on hemicylindrical prisms and two different critical angles were seen in the total internal reflection measurements for (p) and (s) polarized light. This has been predicted to confine 36% of power in the silicon core of a waveguide compared to 2% when vacuum is used as the cladding material in photonic circuits [24, 22, 23].

Future work will involve the fabrication and characterization of more nanostructures and metamaterials so that we can reach the point of having all photonic circuits on chip circuits for faster computation and communication networks.

Bibliography

[1] W. Hendren C. McClatchey R. Atkinson G. Wurtz A. Zayats A. Murphy, J. McPhillips and R. Pollard. The controlled fabrication and geometry tunable optics of gold nanotube arrays. *Nanotechnology*, 22(4), 2011.

[2] R. Azzam and N. Bashara. *Ellipsometry and Polarized Light*. North-Holland Publishing Company, New York, NY, USA, 1977.

[3] M. V. Berry. The adiabatic phase and pancharatnam's phase for polarized light. *Journal of Modern Optics*, 34(11):1401–1407, 1987.

[4] M.V. Berry. Interpreting the anholonomy of coiled light. *Nature*, 326:277–278, 1987.

[5] W. Cai and V. Shalaev. Optical metamaterials: Fundamentals and applications. *Springer Verlag*, 2009.

[6] K. Lai Yi. Chen C. Liu C.Chen, J. Huang and J. He. Giant optical anisotropy of oblique-aligned zno nanowire arrays. *Optics Express*, 20(3), 2012.

[7] W. Chen, M.D. Thoreson, S. Ishii, A.V. Kildishev, and V.M. Shalaev. Ultrathin ultra-smooth and low-loss silver films on a germanium wetting layer. *Optics Express*, 18(5):5124–5134, 2010.

[8] R Chiao and Y. Wu. Manifestations of berry's topological phase for the photon. *Physics Review Letters*, 57(8), 1986.

[9] B. J. Justice S.A. Cummer J.B. Pendry A.F. Starr D Schurig, J.J. Mock and D.R. Smith. Metamaterial electromagnetic cloak at microwave frequencies. *Science*, 314(5801):977–980, 2006.

[10] G. Biener E. Hasman, V. Kleiner and A. Niv. Polarization dependent focusing lens by use of quantized pancharatnam-berry phase diffractive optics. *Applied Physics Letters*, 82(3), 2003.

[11] A. Raman E. Rephaeli and S. Fan. Ultra broadband photonic structures to achieve high-performance daytime radiative cooling. *Nano Letters*, 13(4):1457–1461, 2013.

[12] G. Wiederrecht D. Gosztola V. Podolskiy G. Wurtz, R. Pollard and A. Zayats. Designed ultrafast optical nonlinearity in a plasmonic nanorod metamaterial enhanced by nonlocality. *Nature Nanotechnology*, 6:107–111, 2011.

[13] A.A. Govyadinov and V.A. Podolskiy. Metamaterial photonic funnels for sub diffraction light compression and propagation. *Phys Rev B.*, 73(15):155108, 2006.

[14] R.C. McPhedran G.W. Milton, N.A.P. Nicorovici and V. A. Podolskiy. A proof of superlensing in the quasistatic regime, and limitations of superlenses in this regime due to anomalous localized resonance. *Proc. R. Soc. Math. Phys. Eng. Sci*, 461(2064):3999–4034, 2005.

[15] F. D. M. Haldane. Path dependence of the geometric rotation of polarization in optical fibers. *Optics Letters*, 11(11), 1986.

[16] J. Hao and L. Zhou. Electromagnetic wave scatterings by anisotropic metamaterials: Generalized 4x4 transfer-matrix method. *Physical Review B*, 77(094201), 2008.

[17] R. Wangberg J. Elser and V. Podolskiy. Nanowire metamaterials with extreme optical anisotropy. *Applied Physics Letters*, 89(26), 2006.

[18] M. Rill M. Decker K. Bade V. Saile G. von Freymann S. Linden J. Kansel, M. Thiel and M. Wegner. Gold helix photonic metamaterial as broadband circular polarizer. *Science*, 325(5947), 2009.

[19] Z. Jacob G. Naik A. Boltasseva E. Narimanov J. Kim, V. Drachev and V. Shalaev. Improving the radiative decay rate for dye molecules with hyperbolic metamaterials. *Optics Express*, 20(7), 2012.

[20] M. Jonsson W. Hendren R. Atkinson F. Hook A. Zayats J McPhillips, A. Murphy and R. Pollard. High-performance biosensing using arrays of plasmonic nanotubes. *ACS Nano*, 4(4), 2010.

[21] K. Tsai Z. Li X. Yin G. Bartal A. Stacy Y. Wang J. Yao, Y. Wang and X. Zhang. Design, fabrication and characterization of indefinite metamaterials of nanowires. *Philosophical Transaction of The Royal Society A*, 369(1950), 2011.

[22] S. Jahani and Z. Jacob. Breakthroughs in photonics 2014: Relaxed total internal reflection. *Photonics Journal IEEE*, 7(3), 2014.

[23] S. Jahani and Z. Jacob. Photonic skin-depth engineering. *Journal of the Optical Society of America B*, 32:1346–1353, 2015.

[24] S. Jahani and Z. Jacob. Transparent subdiffraction optics: nanoscale light confinement without metal. *Optica*, 1(2), August 2014.

[25] V. Kleiner K. Bliokh, A. Niv and E. Hasman. Geometrodynamics of spinning light. *Nature Photonics*, 2:748–753, 2008.

[26] M.J. Brett K. Robbie. Sculptured thin films and glancing angle deposition: Growth mechanics and applications. *Journal of Vacuum Science and Technology A-Vacuum Surfaces and Films*, 15(3):1460–1465, 1997.

[27] A. Friedman S. Bennett D. Heiman L. Menon, W. Lu and S. Sridhar. Negative index metamaterials based on metal-dielectric nanocomposites for imaging applications. *Applied Physics Letters*, 93(12), 2008.

[28] S.G. Lipson. Berry's phase in optical interferometry: a simple derivation. *Optics Letters*, 15(3), 1990.

[29] Y. Barnakov D. Dryden G. Nataraj G. Zhu C. Bonner M. Mayy Z. Jacob M. Noginov, H. Li and E. Narimanov. Controllling spontaneous emission with metamaterials. *Optics Letters*, 35(11), 2010.

[30] G.W. Milton and N.A.P. Nicorovic. On the cloaking effects associated with anomalous localized resonance. *Proc. R. Soc. Math. Phys. Eng. Sci*, 462(2074):3027–3059, 2006.

[31] R. Atkinson P. Evans, W. Hendren and R Pollard. Optical transmission measurements of silver, silver-gold alloy and silver-gold segmented nanorods in thin film alumina. *Nanotechnology*, 19(46), 2008.

[32] G. Wurtz W. Dickson A. Murphy F. Morgan R. Pollard I. Iorsh A. Atrashshenko P. Belov Y. Kivshar A. Nevet G. Ankonina M. Orenstein P. Ginzburg, F. Rodriguez Fortuno and A. Zayats. Manipulating polarization of light with ultrathin epsilon-near-zero metamaterials. *Optics Express*, 21(12), 2013.

[33] K. Suresh P. Hariharan, H. Ramachandran and J. Samuel. The pancharatnam phase as a strictly geometric phase: A demonstration using pure projections. *Journal of Modern Optics*, 44(4):707–713, 1977.

[34] J. Atkinson P. Shekhar and Z. Jacob. Hyperbolic metamaterials: Fundamentals and applications. *Nano Convergence*, 1(14), 2014.

[35] S. Pancharatnam. Generalized theory of interference and its applications. *Proceedings of the Indian Academy of Sciences Section A*, 44(5), 1956.

[36] J.B. Pendry. Negative refraction makes a perfect lens. *Physics Review Letters*, 85(18):3966–3969, 2000.

[37] G. Wurtz W. Dickson A. Zayats P. Evans R. Atkinson, W. Hendren and R. Pollard. Anisotropic optical properties of arrays of gold nanorods embedded in alumina. *Physical Review B*, 73(23), 2006.

[38] W. Hendren P. Evans R. Atkinson G. Wurtz R Pollard, A. Murphy and A. Zayats. Optical nonlocalities and additional waves in epsilon-near-zero metamaterials. *Physical Review Letters*, 102(12), 2009.

[39] C. Dewalt S. Molesky and Z. Jacob. High temperature epsillon-near-zero and epsillon-near-pole metamaterial emitters for thermophotovoltaics. *Optics Express*, 21(S1), 2012.

[40] B. Kanchibolta S.Pramanik and S. Bandyopadhyay. *Device Applications of electrochemically self-assembled nanostructures in Handbook of Nanoscience and Nanotechnology.* American Scientific Publishers, Stevenson Ranch, CA, USA, 2008.

[41] R. Starko-Bowes, J. Atkinson, W. Newman, H. Hu, T. Kallos, G. Palikaras, R. Fedosejevs, S. Pramanik, and Z. Jacob. Optical characterization of epsilon-near-zero, epsilon-near-pole, and hyperbolic response in nanowire metamaterials. *Journal of Optical Society of America B*, 32(10):2074–2080, 2015.

[42] A. Tomita and R. Y. Chiao. Observation of berry's topological phase by use of an optical fiber. *Physics Review Letters*, 57(8), 1986.

[43] S. Paskovsky W. Hendren G. Wurtz R. Atkinson R. Pollard V. Podolskiy V. Kabashin, P. Evans and A. Zayats. Plasmonic nanorod metamaterials for biosensing. *Nature Materials*, 8(11), 2009.

[44] P. Evans D. O'Connor R. Atkinson R. Pollard W. Dickson, G. Wurtz and A. Zayats. Dielectric-loaded plasmonic nanoantenna arrays: A metamaterial with tuneable optical properties. *Physical Review B*, 76(11), 2007.

[45] C. Cortes W. Newman and Z. Jacob. Enhanced and directional single-photon emission in hyperbolic metamaterials. *Journal Optical Society of America B*, 30(4), 2013.

[46] V. Kleiner ad E. Hasman Z. Bomzon, G. Biener. Space-variant pancharatnam-berry phase optical elements with computer-generated subwavelength gratings. *Optics Letters*, 27(13), 2002.

[47] L.V. Alekseyev Z. Jacob and E. Narimanov. Optical hyperlens: Far-field imaging beyond the diffraction limit. *Optics Express*, 14(18):8247–8256, 2006.

Appendix A

Appendix 1.0: Effective Medium Theory for a Nanowire System

Here we derive the effective medium parameters for a nanowire system [34]. This method will use the Maxwell-Garnett approach to obtain analytical expressions for the effective permittivity in the parallel ($\epsilon_{\|}$) and perpendicular ($\epsilon_{\perp}$) directions of the nanowire metamaterial. Figure 1.3(b) shows the nature of the embedded metallic nanowires in the surrounding dielectric matrix which have defined permittivities ϵ_m and ϵ_d respectively. Figure 1.4(d) shows an SEM image of a nanowire structure. Furthermore, we will define the fill fraction of nanowires (ρ) in the host material as:

$$\rho = \frac{nanowirearea}{unitcellarea} = \frac{3a}{A} \tag{A.1}$$

The hexagonal unit cell geometry used here consists of 3 nanowires per unit cell (1 centre wire plus additional partial nanowires at each vertex of the hexagon). A is the unit cell area of the hexagon and a is the cross sectional area of a single metallic nanowire.

A.0.1 Effective Parallel Permittivity

In this section we will derive an analytical expression for the parallel component of the permittivity tensor for our nanowire system. We can start from the Schrdinger Wave Equation, which has a solution as a function of the radial distance from the centre of the nanowire (r). We note that at a distance R (the radius of the nanowire) we approach the interface between the metallic wire and dielectric host. We define our potential inside the nanowire as ψ_1 and the potential of the dielectric host as

ψ_2 , we can make the following assertions about the limits of our potential as well as their behaviour at the boundary from known boundary conditions:

$$\psi_1|_{r=R} = \psi_2|_{r=R} \tag{A.2}$$

$$|\psi_1(r=0)| < +\infty \tag{A.3}$$

$$|\psi_2(r \to \infty)| = -E_0 r cos\theta \tag{A.4}$$

$$\epsilon_1 \frac{d\psi_1}{dr}|_{r=R} = \epsilon_2 \frac{d\psi_2}{dr}|_{r=R} \tag{A.5}$$

In equation A.5, ϵ_1 and ϵ_2 are the permittivities inside the metallic nanowire and the dielectric host. We can suggest an arbitrary solution for ψ using a trigonometric series expansion:

$$\psi = A\ln(r) + K + \sum_{n=1}^{\infty} r^n (A_n sin(n\theta) + B_n cos(n\theta)) + \sum_{n=1}^{\infty} \frac{1}{r^n}(C_n sin(n\theta) + D_n cos(n\theta)) \tag{A.6}$$

Now, using our conditions outlined in equations 2-5, we can make approximations to define the potential functions ψ_1 (inside the nanowire) and ψ_2 (outside the nanowire) as the following:

$$\psi_1 = K_1 + \sum_{n=1}^{\infty} r^n (A_n sin(n\theta) + B_n cos(n\theta)) \tag{A.7}$$

$$\psi_2 = K_2 - E_0 r cos(\theta) + \sum_{n=1}^{\infty} \frac{1}{r^n}(C_n sin(n\theta) + D_n cos(n\theta)) \tag{A.8}$$

We can drop the $\frac{1}{r^n}$ term in ψ_1 (A.7) and replace the r^n term in ψ_2 (A.8) with the limit of the potential at

$$\psi_2 \to \infty = -E_0 r cos(\theta) \tag{A.9}$$

This ensures we will get non-infinite solutions for the potentials for all values of r. We can also set the values of the constants K_1 and K_2 in A.7 and equation A.8 to 0. This is due to the fact that when we take the derivative of the potential (ψ) to eventually find our electric fields, these constants will subsequently disappear.

We can now imply our boundary condition given in A.2 for the interface between the nanowire and the dielectric host at R with our defined potentials inside the nanowire (ψ_1) and outside the nanowire (ψ_2). Due to the uniqueness of this

trigonometric series expansion we can say the coefficients of the trigonometric functions for our expression at the boundary are equal.

$$A_n R^n = \frac{C_n}{R^n} \tag{A.10}$$

$$B_n R^n = \frac{D_n}{R^n} \tag{A.11}$$

$$RB_1 = \frac{D_1}{R} - E_0 R \tag{A.12}$$

A.11 is the relation between the coefficients when n =1 in our expansion. We can also write an expression for our second boundary condition given by plugging in A.7 and A.8 into A.5:

$$\epsilon_1 \sum_{n=1}^{\infty} A_n n R^{n-1}(A_n sin(n\theta) + B_n cos(n\theta)) = -\epsilon_2 E_0 cos(\theta) - \epsilon_2 \sum_{n=1}^{\infty} fracn R^{n+1}(C_n sin(n\theta) + D_n cos(n\theta) \tag{A.13}$$

We can once again equate the coefficients of the trigonometric functions given by A.12 to obtain 3 new relations:

$$\epsilon_1 n A_n R^{n-1} = \epsilon_2 \frac{-n}{R^{n+1}} C_n \tag{A.14}$$

$$\epsilon_1 n B_n R^{n-1} = \epsilon_2 \frac{-n}{R^{n+1}} D_n \tag{A.15}$$

$$\epsilon_1 B_1 = -\epsilon_2 E_0 - \epsilon_2 \frac{D_1}{R^2} \tag{A.16}$$

We can set $A_n = B_n = C_n = D_n = 0$ because they are impossible boundary conditions. However, we can still use equation A.11 and A.15 to solve for the coefficients D1 and B1 through substitution:

$$D_1 = \frac{\epsilon_1 - \epsilon_2}{\epsilon_1 + \epsilon_2} R^2 E_0 \tag{A.17}$$

$$B_1 = \frac{-\epsilon_2}{\epsilon_1 + \epsilon_2} E_0 \tag{A.18}$$

A.17 now gives us our expression for B1 which we substitute into our expression for ψ_1 (A.7) at n = 1:

$$\psi_1 = \frac{-2\epsilon_2}{\epsilon_1 + \epsilon_2} E_0 R cos(\theta) \tag{A.19}$$

A.18 now gives us our expression for the potential inside the well in terms of the

electric field outside of the wire ($E_0 = E_{out}$). We can differentiate A.18 with respect to R to get our expression for the electric field inside the nanowire (E_{in}).

$$-\frac{d\psi_1}{dR} = E_{in} = \frac{2\epsilon_2}{\epsilon_1 + \epsilon_2} E_{out} \tag{A.20}$$

The isotropic relation for the parallel permittivity ($\epsilon_\parallel$) with two different material mediums is given by:

$$\epsilon_\parallel = \frac{\rho\epsilon_1 E_{in} + (1-\rho)\epsilon_2 E_{out}}{\rho E_{in} + (1-\rho)E_{out}} \tag{A.21}$$

We will now substitute our expression for E_{in} (A.19) into A.20 and make the substitution that $\epsilon_1 = \epsilon_m$ and $\epsilon_2 = \epsilon_d$ corresponding to the permittivity of the metallic nanorod and dielectric host. Upon making this substitution we arrive at our expression for the parallel component of the permittivity tensor ($\epsilon_\parallel$) in terms of the metallic nanorod fill fraction (ρ) and the permittivities of the nanorod (ϵ_m) and dielectric host (ϵ_d)

$$\epsilon_\parallel = \frac{(1+\rho)\epsilon_m\epsilon_d + (1-\rho)\epsilon_d^2}{(1+\rho)\epsilon_d + (1-\rho)\epsilon_m} \tag{A.22}$$

A.1 Effective Perpendicular Permittivity

We can derive our expression for the perpendicular permittivity from Maxwell's Equations and make use of the electromagnetic boundary conditions. Specifically, we know that the tangential component of the electric field ($E^\perp$) along the long axis of the nanowire is continuous at the interface between the nanowire and the dielectric host.

$$E_1^\perp = E_2^\perp = E^\perp \tag{A.23}$$

where $E_1^\perp$ is the perpendicular electric field in the metallic nanowire, $E_2^\perp$ is the perpendicular electric field in the dielectric host and $E^\perp$ is the effective perpendicular field for the sub wavelength nanowire metamaterial. Note from Maxwell's Equations that the displacement field in the perpendicular direction can be defined as $D^\perp = \epsilon_\perp E^\perp$. We can define our effective perpendicular displacement field by averaging the displacement fields of the metallic nanowires and dielectric host using the metallic fill fraction (ρ).

$$D^\perp = \rho D_1^\perp + (1-\rho)D_2^\perp \tag{A.24}$$

Here $D_1^\perp = \epsilon_m E_1^\perp$ and $D_2^\perp = \epsilon_d E_2^\perp$ correspond to the displacement field of the metallic nanowire and dielectric host respectively. Using these definitions for

the displacement field and subbing in our boundary condition (A.22) into A.23, we arrive at our final expression for the perpendicular permittivity component for our nanowire metamaterial:

$$\epsilon_{\perp} = \rho\epsilon_m + (1-\rho)\epsilon_d \tag{A.25}$$

Appendix B

Appendix 2.0: Effective Medium Theory for a Multilayer System

Here, we will look at deriving the effective medium permittivities for an anisotropic multilayer structure with uniaxial symmetry [34]. The method again follows a generalized Maxwell-Garnett approach to obtain analytical expressions for the effective permittivity in the parallel ($\epsilon_{\parallel}$) and perpendicular ($\epsilon_{\perp}$) directions defined below for the multilayer metamaterial. Figure 1.3(a) shows a schematic of the alternating metallic and dielectric layers to form the multilayer metamaterial. Figure 1.4(c) shows an SEM image of a multilayer structure. The metallic and dielectric layers have permittivities ϵ_m and ϵ_d respectively. Furthermore, we can define the fill fraction of the total thickness of metal in the system to the total thickness of the metamaterial as follows:

$$\rho = \frac{d_m}{d_m + d_d} \tag{B.1}$$

where d_m is the sum of all the thicknesses of metallic layers in the system and d_d is the sum of all the thicknesses of the dielectric layers.

B.0.1 Effective Parallel Permittivity

In this section, we will derive our analytical expression for the parallel component of the permittivity tensor of our multilayer system. We start by noting that the electric field displacement (D) is proportional to the electric field (E) through the following equation:

$$\overrightarrow{D} = \bar{\epsilon_{eff}} \overrightarrow{E} \tag{B.2}$$

where $\bar{\epsilon_{eff}}$ is the overall effective permittivity of the medium. We know from electrostatics that the tangential component of the electric field must be continuous across an interface as we go from one medium to another. Therefore, we have the boundary condition

$$E_m^{\parallel} = E_d^{\parallel} = E^{\parallel} \tag{B.3}$$

where we can take $E_m^{\parallel}$ to be the electric field in the metallic layers, $E_d^{\parallel}$ to be the electric field in the dielectric layers, and $E^{\parallel}$, the electric field of the sub wavelength metamaterial. From the continuity condition of the dielectric displacement in the parallel direction explained above, we can find the overall displacement by averaging the displacement field contributions from the metallic and dielectric components:

$$D^{\parallel} = \rho D_m^{\parallel} + (1-\rho) D_d^{\parallel} \tag{B.4}$$

Substituting B.2 and B.3 to the above, we get:

$$\bar{\epsilon_{eff}^{\parallel}} E^{\parallel} = \rho \epsilon_m E^{\parallel} + (1-\rho)\epsilon_d E^{\parallel} \tag{B.5}$$

If we cancel out the common parallel electric field components, we arrive at the final equation:

$$\epsilon_{\parallel} = \rho \epsilon_m + (1-\rho)\epsilon_d \tag{B.6}$$

B.0.2 Effective Perpendicular Permittivity

To derive our expression for the perpendicular permittivity, we can again start from Maxwell's Equations and use electromagnetic field boundary conditions. We know that the normal component of the electric displacement vector at an interface must be continuous which gives the expression

$$D_m^{\perp} = D_d^{\perp} = D^{\perp} \tag{B.7}$$

We also know that the total magnitude of the electric field will be a superposition of the electric field components from the dielectric layers and the metallic layers. Thus, we can define

$$E^{\perp} = \rho E_m^{\perp} + (1-\rho) E_d^{\perp} \tag{B.8}$$

where $E_m^{\perp}$ is the perpendicular component of the electric field in the metallic region, $E_d^{\perp}$ is the perpendicular component of the electric field in the dielectric region, and $E^{\perp}$ is the total electric field in the multilayer metamaterial. We can now use our boundary condition from B.7 and B.2 and substitute them into B.8.

If we cancel out the common electric field terms and solve for $\epsilon_\perp$, we get the final expression for the electric permittivity of the multilayer metamaterial in the perpendicular direction:

$$\epsilon_\perp = \frac{\epsilon_m \epsilon_d}{\rho\epsilon_d + (1-\rho)\epsilon_m} \tag{B.9}$$